Research Square

Preprints are preliminary reports that have not undergone peer review.
They should not be considered conclusive, used to inform clinical practice,
or referenced by the media as validated information.

Green Extraction of Flavonoids from Cedrus deodara Pollen with Deep Eutectic Solvents and Their Potential Anti-Senescence Properties

wanyu li
Gansu Provincial Academic Institute for Medical Research
Guanjie wu
Gansu Provincial Academic Institute for Medical Research
mian chen
Gansu Provincial Academic Institute for Medical Research
xingmeng zhai
Gansu Provincial Academic Institute for Medical Research
lei kang
Gansu Provincial Academic Institute for Medical Research
guangmiao gao
Gansu Provincial Academic Institute for Medical Research
yawen du
Gansu Provincial Academic Institute for Medical Research
yapeng zhao
Gansu Provincial Academic Institute for Medical Research
gongjian zhu
Gansu Provincial Academic Institute for Medical Research
xiaofeng shi
shixiaofeng2005@sina.com

Gansu Provincial Academic Institute for Medical Research

Article

Keywords: Cedrus deodara pollen, Deep eutectic solvents, Flavonoids, Ozone-induced aging model, SIRT1 signaling, Neuroprotection

Posted Date: September 29th, 2026

DOI: https://doi.org/10.21203/rs.3.rs-10505353/v1

License: This work is licensed under a Creative Commons Attribution 4.0 International License.
Read Full License

Additional Declarations: No competing interests reported.

Green Extraction of Flavonoids from Cedrus deodara Pollen with Deep Eutectic Solvents and Their Potential Anti-Senescence Properties

Wanyu Li[1,2], Guanjie Wu[1,2], Mian Chen[1,2], Xingmeng Zhai[1,2], Lei Kang[1,2], Guangmiao Gao[1,2], Yawen Du[1,2], Yapeng Zhao[1,2], Gongjian Zhu[1,2*], Xiaofeng Shi[1,2*]

[1] Pharmaceutical Research Institute, Gansu Provincial Academic Institute for Medical Research, Lanzhou 730050, China

[2] College of Pharmacy, Gansu University of Traditional Chinese Medicine, Lanzhou 730030, China

E-mail:

Wanyu Li (1057252213@qq.com)

Guanjie Wu (1351026498@qq.com)

Mian Chen (2117694351@qq.com)

Xingmeng Zhai (zxmeng188@163.com)

Lei Kang (3044179023@qq.com)

Guangmiao Gao (guangmiao0929@163.com)

Yawen Du (18811303757@163.com)

Yapeng Zhao (1078417589@qq.com)

Gongjian Zhu (30796076@qq.com)

Xiaofeng Shi (shixiaofeng2005@sina.com)

*Correspondence to: Xiaofeng Shi, Pharmaceutical Research Institute, Gansu Provincial Academic Institute for Medical Research, Xiao Xihu East Street, Lanzhou 730050, China. Tel: 0931-2302664, E-mail: shixiaofeng2005@sina.com

Gongjian Zhu, Department of Science and Education, Gansu Provincial Academic Institute for Medical Research, Xiao Xihu East Street, Lanzhou 730050, China. Tel: 0931-2302513, E-mail: 30796076@qq.com

Abstract: Despite historical claims of anti-aging properties for cedar pollen, its chemical basis and mechanisms remain unclear. This study optimized a deep eutectic solvent (DES) extraction of total flavonoids from Cedrus deodara pollen and evaluated their anti-aging effects in an ozone-induced mouse model. A choline chloride-1,3-butanediol DES system was optimized via response surface methodology. C57BL/6 mice were exposed to ozone (2.0 ppm, 1 h/day) and administered cedar pollen (1.25 g/kg) or total flavonoid extracts (50, 100, 200 mg/kg) for 14 days. Assessments included Morris water maze, serum oxidative stress markers, histopathology (H&E, Nissl, SA-β-gal), LC-MS/MS flavonoid profiling, molecular docking against SIRT1, and RT-qPCR of Sirt1, PGC-1α, and mTOR. The optimized extraction yielded (45.97 ± 1.29) mg/g total flavonoids purity (21.19 ± 1.15)%, with 45 compounds identified. Flavonoid treatment significantly improved spatial memory, elevated SOD, GSH and T-AOC, reduced MDA, attenuated hippocampal and pulmonary damage, and lowered SA-β-gal positivity. All 45 flavonoids showed favorable SIRT1 binding (-7.05 to -10.83 kcal/mol), with qPCR confirming upregulated Sirt1-PGC-1α and downregulated mTOR. DES-based extraction effectively enriches bioactive flavonoids from cedar pollen, which exert neuroprotective anti-aging effects in vivo via Sirt1-PGC1α and Sirt1-mTOR modulation. These findings support cedar pollen flavonoids as functional food candidates against age related cognitive decline.

Keywords： Cedrus deodara pollen; Deep eutectic solvents; Flavonoids; Ozone-induced aging model; SIRT1 signaling; Neuroprotection

Introduction

The global demographic shift toward an aging population has imposed substantial burdens on healthcare systems, social welfare programs, and labor markets worldwide [1,2]. This unprecedented increase in the elderly demographic is accompanied by a rising prevalence of age-associated disorders, including neurodegenerative diseases, cardiovascular pathologies, and musculoskeletal degenerative conditions, thereby posing formidable challenges to public health infrastructure [3-5]. Elucidating the fundamental mechanisms underlying aging is a prerequisite for understanding the etiology of these chronic diseases and for

developing effective preventive and therapeutic strategies. Consequently, ensuring healthy, active, and dignified aging has emerged as a critical societal priority, and the identification of novel interventions, including nutraceuticals and pharmacological agents capable of delaying aging or mitigating its associated pathologies has become a central focus of biomedical research [6-8].

Among the various natural compounds investigated for their antiaging properties, flavonoids have attracted widespread attention [9,10]. Their potent free radical scavenging activity and capacity to alleviate oxidative stress confer marked advantages, positioning them as promising candidates not only for delaying systemic aging and counteracting cutaneous photoaging, but also for exerting beneficial effects on age-related chronic conditions, including diabetes, neurodegenerative disorders, and osteoporosis [11-14]. Historical records from ancient China attest to the recognized medicinal value of pine pollen. The Newly Revised Materia Medica (Xinxiu Bencao) documents that prolonged consumption of pine pollen "lightens the body" and that its therapeutic efficacy surpasses that of pine bark, pine needles, or pine resin, marking the earliest recorded claim of its superior health benefits. The Compendium of Materia Medica (Bencao Gangmu) further describes its actions as "moistening the heart and lungs, supplementing vital qi, dispelling wind, and arresting bleeding," and notes its suitability for wine brewing. In contemporary practice, China's National Health Commission (Announcement No. 17, 2014) explicitly listed pine pollen among ten pollen types approved for use as general foodstuffs, underscoring its favorable safety profile and dual applicability as both a food and a dietary supplement. Modern pharmacological studies have further revealed that pine pollen contains a diverse array of bioactive constituents, including sterols, flavonoids, amino acids, and trace elements, which exhibit antioxidant, hypoglycemic, hepatoprotective, and potential anti-aging activities [15,16]. These findings collectively support its continued investigation as a functional food and potential therapeutic agent.

The present study was undertaken to evaluate the antiaging potential of cedar pollen, a source of pine pollen. Although our preliminary ethanol-based extraction of total flavonoids from cedar pollen yielded promising in vitro antioxidant activity [17],

the conventional method suffered from low yield and purity, hindering further investigation. To address this limitation, we turned to deep eutectic solvents (DESs), which is a green, easily prepared, and biodegradable multicomponent systems stabilized by hydrogen bonding networks between hydrogen bond donors (e.g., urea, carboxylic acids) and acceptors (e.g., quaternary ammonium salts). DESs have been widely adopted across pharmaceutical, materials science, and chemical engineering applications [18]. including metal recovery from industrial effluents [19], detection of analytes in food and packaging materials [20-22], and extraction of radioactive elements [23,24]. Within the domain of traditional Chinese medicine, DESs have proven particularly effective for the selective and efficient extraction of flavonoids and phenolic acids from medicinal plants [25-28], owing to the presence of unsaturated groups and hydrogen-bonding moieties in these target compounds. This evidence provides a strong rationale for employing DES-based extraction in the current study to obtain higher quality flavonoid fractions. Accordingly, we optimized the DES extraction process for cedar pollen preparation.

For in vivo evaluation, C57BL/6 mice were selected as the experimental model. Although oxidative stress-based aging models most commonly established via D-galactose injection or H_2O_2 treatment are widely adopted, they are often associated with prolonged induction periods and potential irreversible tissue damage [29,30]. As an alternative, ozone-induced oxidative stress has been shown to effectively trigger aging related phenotypes with a shorter modeling time and milder impact on general phenotypic deterioration [31,32]. This approach was initially validated in 1994, when ozone exposure was reported to elevate malondialdehyde (MDA) levels in mouse brain tissue and impair learning and memory functions [33]. More recently, accumulating evidence has demonstrated that ozone induced models can recapitulate aging-associated neuronal damage, suggesting their utility in studying neurodegenerative processes exacerbated by aging. Based on this rationale, the present study adopted ozone exposure to establish an aging mouse model. Vitamin C was used as the positive control [34-36], and the experimental groups comprised a blank control, a model group, a positive control group, a cedar pollen group, and low-,

medium-, and high-dose total flavonoid extract groups. Drug administration was initiated concurrently with ozone exposure. After modeling, spatial learning and memory were assessed using the Morris water maze test, after which serum, brain, and lung tissues were collected. Biochemical analyses included oxidative stress biomarkers, hematoxylin eosin (HE) histopathological examination, hippocampal neuronal counting, and senescence associated β-galactosidase (SA-β-gal) staining of brain tissue. Collectively, these parameters enabled a systematic assessment of the antiaging potential of cedar pollen and its total flavonoid extract, with emphasis on their capacity to alleviate oxidative damage and mitigate aging related neurodegenerative alterations.

Conventional network pharmacology approaches, though useful for broadly predicting potential mechanisms and signaling pathways, tend to yield highly diverse and functionally pleiotropic compound target interactions that complicate precise mechanistic dissection. To circumvent this limitation, we directly employed molecular docking against key signaling molecules, thereby enabling a more focused preliminary exploration of the underlying mechanisms. Specifically, we centered our attention on Sirt1, a well-recognized aging-related molecular target. Sirtuins are a family of NAD^+ dependent enzymes that sense intracellular energy status and metabolic signals, regulate mitochondrial dysfunction, and exert neuroprotective effects, thereby modulating the progression of age associated diseases [37]. Flavonoids have been reported to mitigate cellular senescence by upregulating Sirt1 activity and expression. Within the Sirt1-PGC1α axis, peroxisome proliferator-activated receptor gamma coactivator 1-alpha (PGC1α) serves as a master transcriptional coactivator governing mitochondrial biogenesis and homeostasis. Sirt1 deacetylates PGC1α, thereby enhancing mitochondrial biosynthesis and oxygen consumption, which collectively contribute to the retardation of aging. Additionally, Sirt1 has been shown to delay aging through inhibition of the mTOR pathway and subsequent activation of autophagy, as mTOR suppression is known to extend lifespan across multiple model organisms [38]. Based on this mechanistic rationale, we conducted a preliminary investigation into the antiaging mechanisms of cedar pollen and its total flavonoid

extract, with particular emphasis on the Sirt1-PGC1α and Sirt1-mTOR signaling cascades.

In summary, this study established an optimized DES-based extraction protocol for total flavonoids from cedar pollen, evaluated its neuroprotective and cognitive enhancing effects in an ozone-induced aging mouse model, and performed qPCR analysis to preliminarily explore the involvement of Sirt1 related pathways. Collectively, these findings provide a practical reference for the efficient extraction of cedar pollen flavonoids and offer experimental evidence supporting its potential as an antiaging agent with neuroprotective properties. Nevertheless, further studies are warranted to identify the specific active constituents and to fully elucidate the molecular cascades governing the observed effects.

Results

Results of the methodological evaluation of the total flavonoid content determination method

The regression equation for the total flavonoid content determination method was found to be $y = 0.00227x + 0.00138$ ($r = 0.9993$), indicating a good linear relationship within the concentration range of 12.28 μg/mL to 73.68 μg/mL. The RSD of the precision test results was 2.81%, indicating good precision of the instrument; The RSD for the repeatability test was 2.46%, indicating good repeatability of the method; the RSD for the stability test was 1.93%, indicating good stability of the sample solution over 24 hours; the spiked recovery test results showed a spiked recovery rate of 106.4% with an RSD of 2.82%, indicating that the method is accurate and stable.

Screening Results for DES Solvent Hydrogen Bond Donor and Acceptor Compounds

Using total flavonoid content as the evaluation metric, a systematic screening of DES with varying molar ratios of HBA to HBD was performed. Among the tested combinations, the choline chloride-1,3-butanediol system exhibited the highest extraction efficiency for total flavonoids from Cedrus deodara pollen. Consequently,

this HBA-HBD combination was selected and employed in all subsequent extraction experiments, as shown in Figure 1A.

Results of the Study on Factors Affecting DES Extraction

Figure 1B illustrates the effect of different molar ratios of choline chloride and 1,3-butanediol on extraction efficiency. The results indicate that the best extraction efficiency is achieved at a molar ratio of 1:2 for HBA-HBD; therefore, a 1:2 molar ratio was selected as the condition for subsequent experiments. Figure 1C illustrates the effect of the moisture content in the DES system on extraction efficiency. The results indicate that extraction efficiency is highest at a moisture content of 20%; however, as the moisture content increases, extraction efficiency drops sharply when it exceeds 40%. This may be due to excessively high moisture content affecting the properties of the DES components, disrupting the hydrogen bond structure within the DES, and thereby impairing the dissolution of flavonoids. Figure 1D illustrates the effect of the liquid-to-solid ratio on extraction efficiency. The results indicate that extraction efficiency gradually decreases as the liquid-to-solid ratio increases. This may be because, as the liquid-to-solid ratio increases, the elution of compounds other than flavonoids from cedar pollen also increases, competitively inhibiting the elution of flavonoids and leading to reduced extraction efficiency. Figure 1E illustrates the effect of extraction temperature on extraction efficiency. As the extraction temperature increases, the total flavonoid content gradually rises. Short term heating during extraction helps reduce the viscosity and surface tension of the DESs used, thereby facilitating the elution of active components from the plant material. Figure 1F illustrates the effect of extraction time on extraction efficiency. The results indicate that when the initial extraction time is short, the impact of extraction time on efficiency is negligible; however, when the extraction time is too long, extraction efficiency decreases. This may be due to structural changes in some flavonoids caused by prolonged heating at excessively high temperatures, or it may be because the elution of other compounds competitively inhibits the elution of flavonoids.

Based on the results of the single-factor experiments, since there was little difference in extraction efficiency under molar ratios of 1:1, 1:2, and 1:3, but

extraction efficiency decreased significantly at ratios of 2:1 and 3:1, molar ratios of 1:1, 1:2, and 1:3 were selected as the factors and levels for the response surface experiment. Since moisture content had a significant impact on extraction efficiency, a fixed moisture content of 20% was established as the reaction condition, and no further screening of moisture content under other conditions was conducted. The extraction efficiency was optimal at a liquid-to-solid ratio of 5:1. Given the cost of DES reagents, a liquid-to-solid ratio of 5:1 was fixed as the reaction condition to balance cost and extraction efficiency. Extraction efficiency increased gradually within the temperature range of 60 °C to 80 °C, and temperature significantly influenced extraction efficiency. Therefore, extraction temperatures of 60 °C, 70 °C, and 80 °C were selected as the factors and levels for the response surface experiment. Extraction times of 10 min, 15 min, and 20 min yielded good extraction results with no significant differences; however, extraction times exceeding 20 min incur higher costs. After comprehensive consideration, 10 min, 15 min, and 20 min were selected as the factors and levels for the response surface experiment.

Optimization results from the response surface obtained using DES

We employed response surface methodology to conduct a comprehensive multivariate analysis and optimize the extraction process. As shown in the results in Table 1, the model is significant, while the residual term is not significant, indicating that the model was successfully established; The regression equation is $R_1 = 35.82 + 1.11A + 2.54B - 0.55C + 0.44AB - 0.67AC - 0.65BC + 3.56A^2 + 0.26B^2 + 1.22C^2$, with $R^2 = 0.9006$, $R^2_{(ADJ)} = 0.7728$, CV% = 3.76, indicating that the model has a high degree of fit. The first order factor B (extraction temperature) is significant, indicating that extraction temperature has a significant effect on extraction efficiency; the second order term A^2 is significant, indicating that the molar ratio has a nonlinear effect on extraction efficiency; none of the interaction effects are significant, indicating that interactions have a minor effect on extraction efficiency. The three-dimensional response surface plot showing the effects of interactions among the factors on the extraction process is shown in Figure 1(G, H, I).

Analysis using Design Expert V8.0.6.1 software determined that the optimal

process for extracting total flavonoids from cedar pollen using DES is: A(molar ratio) = 0.99, B(extraction temperature) = 0.95, and C(extraction time) = -0.51. For operational feasibility and convenience, the final extraction process was established as follows: a molar ratio of choline chloride to 1,3-butanediol of 1:3, an extraction temperature of 80 °C, and an extraction time of 12 min. Validation results from three batches showed that the total flavonoid content of cedar pollen extracted under these conditions was (45.97±1.29) mg/g, with an RSD of 2.80%, indicating that this optimal extraction process is stable and feasible for the extraction of total flavonoids from cedar pollen.

Tab.1 Box-Behnken Design and Results (n=3)

Std	**Run**	**Factor1**	**Factor2**	**Factor2**	**R1**
		A	**B**	**C**	**mg/g**
6	1	1	0	-1	42.2315
5	2	-1	0	-1	40.6793
4	3	1	1	0	44.4280
8	4	1	0	1	39.1634
17	5	0	0	0	33.9094
1	6	-1	-1	0	35.7264
7	7	-1	0	1	40.2758
15	8	0	0	0	36.0093
3	9	-1	1	0	39.3330
16	10	0	0	0	36.4938
11	11	0	-1	1	34.8771
14	12	0	0	0	35.9285
10	13	0	1	-1	41.0140
2	14	1	-1	0	39.0433
12	15	0	1	1	39.2492
9	16	0	-1	-1	34.0234
13	17	0	0	0	36.7361

Tab.2 Analysis of Variance Table

Source	Sum of Squares	df	Mean Square	F Value	p-value Prob＞F	
Model	131.00	9	14.56	7.05	0.0087	significant
A	9.79	1	9.79	4.74	0.0659	
B	51.79	1	51.79	25.07	0.0016	significant
C	2.40	1	2.40	1.16	0.3167	
AB	0.79	1	0.79	0.38	0.5558	
AC	1.78	1	1.78	0.86	0.3848	
BC	1.71	1	1.71	0.83	0.3926	
A^2	53.27	1	53.27	25.79	0.0014	
B^2	0.29	1	0.29	0.14	0.7211	
C^2	6.22	1	6.22	3.01	0.1263	
Residual	14.46	7	2.07			
Lack of Fit	9.47	3	3.16	2.53	0.1958	
Pure Error	4.99	4	1.25			
Cor Total	145.46	16				

Results of In Vitro Antioxidant Evaluation of DES Total Flavonoid Extract

The results indicate that the DES total flavonoid extract from cedar pollen exhibits good in vitro antioxidant activity. Ascorbic acid was used as the positive control, see Figure 3(A, B, C), which show the scavenging effects of the extract on DPPH radicals, ABTS radicals, and OH^- radicals, respectively. The IC_{50} values for the scavenging of DPPH, ABTS, and OH^- radicals are shown in Table 3.

Tab.3 IC_{50} values of total flavonoids for different free radical scavenging activities (n=3)

Category	$IC_{50}(\bar{x}\pm s)$ μg/mL
DPPH radicals	121.51±2.09
ABTS radicals	31.71±1.50
OH^- radicals	151.19±2.18

Results of Fourier Transform Infrared Spectroscopy Analysis

Figure 3D shows the infrared spectrum of the DES extraction solvent. 1 indicates a strong, broad absorption band at 3500-3200 cm^{-1} in the DES extraction solvent, reflecting the enrichment of hydrogen-bonding structures. This demonstrates a core characteristic of DES strong hydrogen bonding making this peak highly prominent. 2 indicates an absorption peak at 3000-2800 cm^{-1}, corresponding to C-H stretching vibrations (e.g., $-CH_2-$ and $-CH_3$ in saturated alkanes). This originates from the alkyl chains in hydrogen bond acceptors such as choline chloride and is also one of the signature peaks of DES. 3 indicates an absorption band at 1650-1600 cm^{-1}, corresponding to H-O-H bending vibrations, which originate from water in the DES or from the bending vibrations of hydroxyl groups in hydrogen bond donors.

Figure 3E shows the infrared spectrum of the 75% ethanol extract. 1 indicates an absorption band at 3500-3200 cm^{-1}, suggesting the presence of -OH groups. 2 indicates an absorption peak at 3000-2800 cm^{-1}, corresponding to C-H stretching vibrations (e.g., $-CH_2$ and $-CH_3$ in saturated alkanes), which are presumed to originate from the side chains of flavonoids, the cycloalkane structures of some flavonoids and phenolic acids, and the alkyl groups in the ethanol solvent. 3 indicates an absorption near 1700 cm^{-1}, where the strong absorption peak corresponds to C=O stretching vibrations, supporting the presence of carboxylic acid/ester groups in flavonoids and phenolic acid derivatives. 4 indicates an absorption at 1650-1600 cm^{-1}, corresponding to C=C stretching vibrations (e.g., aromatic rings, double bonds). This is a typical region for vibrations of the benzene ring skeleton in flavonoids and may also originate from H-O-H bending vibrations of water in the sample.

Figure 3F shows the infrared spectrum of the DES extract. 1 indicates a strong, broad absorption band at 3500-3200 cm^{-1}, which is a typical signal of O-H stretching vibrations. This band originates from the polyhydroxy and polyol hydroxyl structures of flavonoids and phenolic acids, as well as the strong hydrogen-bonding network and residual water in the DES solvent itself. 2 indicates an absorption near 1700 cm^{-1}, where the strong absorption peak corresponds to C=O stretching vibrations, supporting the presence of carboxylic acid/ester groups in the flavonoid and phenolic acid derivatives. 3 indicates absorption in the 1650-1600 cm^{-1} range, corresponding to

C=C stretching vibrations (e.g., aromatic rings, double bonds). This is a typical region for vibrations of the benzene ring skeleton in flavonoid compounds and may also originate from H-O-H bending vibrations of water in the sample.

Infrared characterization of the DES extract revealed characteristic peaks such as O-H, C=O, and C-O, which closely match the structures of flavonoids and phenolic acids, indicating that DES successfully extracted the target bioactive compounds. A comparison with the infrared spectrum of the 75% ethanol extract shows that the O-H peak is broader and stronger, suggesting the formation of a stronger hydrogen bond network between the extract and DES. The peak shapes in the 1500-500 cm^{-1} fingerprint region are more complex, reflecting the diversity of the DES extraction solvent and the DES extract.

Scanning electron microscopy analysis results

Figure 2(A, B) shows scanning electron microscope images of cedar pollen before and after wall lysis, respectively. Unlysed pollen grains are nearly spherical or ellipsoidal, exhibiting a typical “pine-type” structure consisting of a central body flanked by two air sacs. The air sacs are extensions of the pollen wall; they are filled with air and, like “wings” or the cap of a mushroom, help the pollen float in the air, facilitating wind mediated pollination. At 1000× magnification, the pollen grain surface clearly exhibits a rough, granular or microvillous texture, which is a key identifying characteristic of pine pollen. Based on the scale bar, the diameter of the pollen body is estimated to be approximately 30-50 μm; including the lateral air sacs, the total length can reach 60-80 μm, consistent with the typical size range of pine pollen. In intact pine pollen grains, the typical bicellular structure is preserved, with clear surface texture on the pollen wall and only minor damage at the junction between the air sacs and the main body; in ruptured pine pollen grains, the bicellular structure has completely collapsed and fused, the contours of the air sacs have disappeared, and the pollen wall exhibits distinct cracks and folds, with a rough surface, displaying typical characteristics of deep rupture.

Figure 2(C, D) shows scanning electron microscope images of pine pollen grains following heat extraction with 75% ethanol and DES extraction, respectively. After

heat extraction with 75% ethanol, the pollen grain structure was severely damaged; a large number of grains appeared shriveled, fragmented, collapsed, or agglomerated, with rough surfaces and severely disrupted textures. Obvious pores and damage were visible, and some areas exhibited indentations left by the leaching of substances. Following DES extraction, the pollen grain structure remains relatively intact. Most grains retain their basic spherical or elliptical contours, and the double vessel structure is more clearly identifiable. Although some wrinkling and deformation are present, fragmentation and agglomeration are less common. The surface texture is relatively clear; while minor creasing is observed, there are no large scale fractures or cavities, and the traces of substance leaching are more subtle. It can thus be concluded that ethanol disrupts pollen structure through intense swelling, whereas DES achieves selective extraction via mild hydrogen bonding, exerting a gentler effect on the structure. While effectively eluting the target components, DES causes significantly less damage to the pollen grain structure.

Results of the Evaluation of DES Recovery Performance

An examination of the adsorption rates of different resins, as shown in Figure 3G, revealed that DM-130 resin exhibited the highest adsorption rate for flavonoids in the DES extract. Therefore, DM-130 resin was ultimately selected for the adsorption of flavonoids from the DES extract. The results of the study on the volume of the adsorbent solution are shown in Figure 3H. Although the adsorption rate was highest at a 1:1 volume ratio, considering cost and the fact that there was no significant difference in adsorption rates between the 1:1 and 2:1 volume ratios, a 2:1 volume ratio of DES extract was selected for subsequent experiments to conserve resources. The results of the adsorption time study are shown in Figure 3I. As the volume of the extract solution increased, an 8-hour adsorption period did not result in more complete or increased adsorption of the flavonoids. As the adsorption time was extended, the adsorption rate gradually increased, reaching its peak at 24 hours. To avoid over-adsorption of the components and considering both adsorption efficiency and operational simplicity, we ultimately determined that 24 hours is the optimal adsorption time.

Based on the comprehensive experimental results, when using DM-130 macroporous adsorption resin, adding an extraction solution equal to twice the volume of the resin, and allowing for static adsorption for 24 hours, the resin demonstrated the best adsorption performance for the flavonoid components in the DES extraction solution. Since the results of the previously optimized alcohol extraction process indicated that 75% ethanol yielded the best extraction results, and although anhydrous ethanol demonstrated good desorption performance, its high operational cost made it less favorable for the subsequent recovery of the flavonoid components. Therefore, we examined the dynamic desorption performance of both anhydrous ethanol and 75% ethanol. The results showed that the purity of the anhydrous ethanol desorption solution was (18.92±0.83)%, while the purity of the 75% ethanol desorption solution was (21.19±1.15)%. The 75% ethanol desorption solution exhibited higher flavonoid purity, and following dynamic desorption, the desorption rate of the 75% ethanol solution increased to (71.27±0.58)%, with a recovery rate of (67.90±0.50)%.

Results of the Analysis of Non-Target Metabolites in DES Extracts

Non-targeted metabolomic analysis was performed using UPLC-MS/MS on the original plant material and DES extracts of cedar pollen. A total of 13 classes of compounds were identified. Compared with the plant material, the DES extraction resulted in a significant increase in both the variety and content of terpenoids and flavonoids in the extract (Figure 4A), indicating that the properties of the DES extraction solvent are suitable for the extraction and preparation of compounds rich in hydrogen bonds and unsaturated functional groups.

Non-targeted metabolomic analysis revealed that the retention times of detected compounds in both positive- and negative-ion modes were predominantly distributed within the range of 4-12 min (Figure 4B), suggesting that the DES extract is enriched in moderately polar constituents. This retention window typically encompasses compound classes such as flavonoids, phenolic acids, alkaloids, and moderately polar terpenoids, which is consistent with our preliminary expectations. Notably, while the positive ion mode produced detectable mass spectrometric signals for the majority of compounds, the overall chromatographic resolution remained suboptimal. In contrast,

the negative ion mode exhibited superior detection performance, with substantially higher enrichment and sensitivity for phenolic acids, flavonoids, organic acids, saponins, and tannins.

Results of Quantitative Metabolomic Analysis of Flavonoids in DES Extracts

Quantitative analysis of flavonoids revealed a total of 45 flavonoid compounds in the DES extracts Figure 4(C, D). See Table 4 for the correlation equations and correlation coefficients associated with the compound detection.

Tab.4 Linear Relationships for the Quantitative Analysis of Flavonoid Compounds

No.	Compound	Equation	Relevance (r)
1	Luteolin-7-β-D-glucuronide	$y=8.7755\times10^{-4}x+3.72327\times10^{-4}$	0.99903
2	Hyperoside	$y=5.73435\times10^{4}x+3.61059\times10^{4}$	0.99787
3	5-Methyl-7-methoxyisoflavone	$y=5.68170\times10^{5}x+9.33344\times10^{4}$	0.99689
4	Biochanin A	y=16307.35129x+8558.31862	0.99345
5	6-Methoxyflavone	y=0.02510x+0.00612	0.99855
6	Naringenin chalcone	$y=3.77983\times10^{-4}x+0.01211$	0.99936
7	4',7-Di-O-methylnaringenin	y=28104.17164x+4301.41696	0.99765
8	Pinobanksin	y=0.00654x+0.18322	0.99883
9	Apiin	y=0.00723x+0.00118	0.99583
10	Hydroxygenkwanin	y=0.00900x+0.00754	0.99910
11	Naringenin	y=0.00266x+0.09480	0.99711
12	Norartocarpetin	$y=7.65306\times10^{-4}x+3.47480\times10^{-4}$	0.9997
13	6-Methoxyluteolin	$y=0.00126x+7.27417\times10^{-4}$	0.99451
14	Apigenin-4'-O-glucoside	$y=0.00318x+8.25184\times10^{-4}$	0.99534
15	Luteolin	$y=7.65306\times10^{-4}x+3.47480\times10^{-4}$	0.99970
16	Isorhamnetin	y=0.00290x+0.00110	0.99758
17	Quercetin-3-O-β-D-Glucuronide	$y=6.25179\times10^{-4}x-1.24406\times10^{-4}$	0.99262
18	Quercetin-3-O-sophorose	$y=6.98136\times10^{-4}x+3.15057\times10^{-4}$	0.99951
19	Narcissoside	$y=5.25617\times10^{-4}x+1.90303\times10^{-4}$	0.99870
20	Isorhamnetin-3-O-glucoside	y=11676.00711x-3619.65340	0.99948

21	Isorhamnetin-3-O-galactoside	y=11676.00711x-3619.65340	0.99948
22	Myricetin	$y=0.00356x-3.71202\times10^{-4}$	0.99862
23	Tiliroside	y=0.00585x+0.00112	0.99896
24	Tamarixin	y=11676.00711x-3619.65340	0.99948
25	Puerarin	$y=0.00285x-2.99103\times10^{-4}$	0.99624
26	Sophoricoside	$y=0.00318x+8.25184\times10^{-4}$	0.99534
27	Sophorobioside	$y=7.28399\times10^{-4}x+7.53752\times10^{-5}$	0.99275
28	Diosmetol-7-glucoside	$y=5.73325\times10^{-4}x+1.86978\times10^{-4}$	0.99737
29	Apigenin-7-glucoside	$y=0.00121x-1.68669\times10^{-4}$	0.99994
30	Thermopsoside	$y=5.73325\times10^{-4}x+1.86978\times10^{-4}$	0.99737
31	Phloretin	$y=0.00241x+9.72095\times10^{-4}$	0.99783
32	(-)-Catechin	$y=2.95834\times10^{-4}x+8.77408\times10^{-4}$	0.99612
33	Afzelechin	$y=5.40439\times10^{-4}x-1.91754\times10^{-4}$	0.99722
34	Eriocitrin	y=0.00880x-0.01519	0.99645
35	Poncirin	$y=0.00319x-5.15713\times10^{-4}$	0.99928
36	Didymin	$y=0.00319x-5.15713\times10^{-4}$	0.99928
37	Isosakuranetin	$y=0.00163x+7.61845\times10^{-4}$	0.99937
38	Hesperetin-5-O-glucoside	$y=4.7946\times10^{-4}x+1.68101\times10^{-4}$	0.99675
39	Eriodictyol	$y=1.40953\times10^{-4}x-2.02704\times10^{-4}$	0.99830
40	Dihydrokaempferol	$y=0.00187x+5.47307\times10^{-4}$	0.99797
41	Taxifolin	$y=4.24927\times10^{-4}x+2.63331\times10^{-4}$	0.99848
42	Diosmetin	y=0.01006x+0.00199	0.99739
43	Cynaroside	y=0.00437x+0.00422	0.99577
44	Scutellarin	y=0.00633x+0.00263	0.99175
45	Chrysoeriol	y=0.01006x+0.00199	0.99739

The ionization modes, retention times, and quantified concentrations of the identified flavonoids are summarized in Table 5. Among these compounds, five groups of isomers were distinguished based on their structural features. These include: (1) tautomers, exemplified by naringenin chalcone and naringenin; (2) methoxy positional isomers, represented by diosmetin and chrysoeriol, as well as isorhamnetin

and tamarixetin; (3) glycosidic linkage positional isomers, such as apigenin 4'-O-glucoside and apigenin 7-glucoside; and (4) glycosidic diastereoisomers, exemplified by isorhamnetin-3-O-glucoside and isorhamnetin-3-O-galactoside. Given that chromatographic separation and unambiguous structural characterization remain challenging for these isomeric pairs, further optimization of the UPLC conditions, in conjunction with NMR spectroscopic analysis, is warranted to conclusively determine their absolute configurations.

The identified compounds were classified as flavonoids and further categorized into five subclasses based on their structural backbones. As summarized in Table 5, these included flavonoids (compounds 15, 1, 43, 14, 9, 29, 30, 5, 13, 45, 42, 28, 12, 10, and 44), flavanols/dihydroflavanols (2, 17, 18, 16, 20, 21, 19, 22, 23, 27, 24, 8, 40, and 41), dihydroflavones (11, 6, 7, 39, 34, 35, 36, 37, and 38), isoflavones (3, 4, 25, and 26), flavanols (32 and 33), and chalcones/dihydrochalcones (6 and 31). The flavonoid and flavanol subclasses constituted the predominant components of the DES extract, indicating their major contribution to the overall flavonoid profile, Since there are a large number of compounds, we selected secondary mass spectra of several representative components by category (Figure 4D) to illustrate.

Based on their aglycone skeletons, the identified flavonoid glycosides were categorized into nine groups. As detailed in Table 5, these included luteolin (compounds 15, 1, and 43), apigenin (14, 29, and 30), quercetin (2, 17, and 18), isorhamnetin (16, 20, 21, and 19), naringenin (11, 6, 35, and 7), eriodictyol (39 and 34), diosmetin (42 and 28), kaempferol (23 and 27), and isosakuranetin (37 and 36). In addition, several free flavonoid aglycones were also detected in the extract, indicating the presence of both glycosylated and non-glycosylated flavonoid forms in the DES derived profile.

Tab.5 Quantitative Analysis of Flavonoid Content

No.	Compound	Category	Ion Mode	RT (min)	Content (μmol/L)
1	Luteolin-7-β-D-glucuronide	Flavone glycoside	[M+H]+	2.72	0.025569

2	Hyperoside	Flavonol glycoside	[M+H]+	2.68	0.00537
3	5-Methyl-7-methoxyisoflavone	Isoflavone	[M+H]+	12.7	0.000611
4	Biochanin A	Isoflavone	[M+H]+	9.39	0.012935
5	6-Methoxyflavone	Flavone	[M+H]+	10.37	0.001754
6	Naringenin chalcone	Chalcone	[M+H]+	5.29	7.060746
7	4',7-Di-O-methylnaringenin	Flavanone	[M+H]+	12.32	0.017929
8	Pinobanksin	Flavanone	[M+H]+	5.29	2.581469
9	Apiin	Flavone glycoside	[M+H]+	2.85	0.001299
10	Hydroxygenkwanin	Flavone	[M+H]+	7.16	0.000188
11	Naringenin	Flavanone	[M+H]+	2.72	3.135517
12	Norartocarpetin	Flavanone	[M-H]-	4.25	0.008204
13	6-Methoxyluteolin	Flavone	[M-H]-	4.38	0.0089
14	Apigenin-4'-O-glucoside	Flavone glycoside	[M-H]-	3.02	0.017296
15	Luteolin	Flavone	[M-H]-	4.25	0.008204
16	Isorhamnetin	Flavonol	[M-H]-	5.84	0.039924
17	Quercetin-3-O-β-D-Glucuronide	Flavonol glycoside	[M-H]-	2.71	0.006087
18	Quercetin-3-O-sophorose	Flavonol glycoside	[M-H]-	2.37	0.016213
19	Narcissoside	Flavonol glycoside	[M-H]-	2.8	0.018228
20	Isorhamnetin-3-O-glucoside	Flavonol glycoside	[M-H]-	2.97	0.141051
21	Isorhamnetin-3-O-galactoside	Flavonol glycoside	[M-H]-	2.97	0.141051
22	Myricetin	Flavonol	[M-H]-	3.34	0.010559
23	Tiliroside	Flavonol glycoside	[M-H]-	4.02	0.021563
24	Tamarixin	Flavonol glycoside	[M-H]-	2.97	0.141051
25	Puerarin	Isoflavone glycoside	[M-H]-	2.23	0.003765
26	Sophoricoside	Isoflavone glycoside	[M-H]-	3.02	0.017296
27	Sophorobioside	Isoflavone glycoside	[M-H]-	2.89	0.012059

28	Diosmetol-7-glucoside	Flavone glycoside	[M-H]-	3.1	0.002013
29	Apigenin-7-glucoside	Flavone glycoside	[M-H]-	3.02	0.018772
30	Thermopsoside	Flavonol glycoside	[M-H]-	3.1	0.002013
31	Phloretin	Dihydrochalcone	[M-H]-	5.24	0.031146
32	(-)-Catechin	Flavan-3-ol	[M-H]-	2.18	0.757466
33	Afzelechin	Flavan-3-ol	[M-H]-	2.48	0.973477
34	Eriocitrin	Flavanone glycoside	[M-H]-	2.58	0.022118
35	Poncirin	Flavanone glycoside	[M-H]-	4.01	0.027021
36	Didymin	Flavanone glycoside	[M-H]-	4.01	0.027021
37	Isosakuranetin	Flavanone	[M-H]-	8.86	0.00447
38	Hesperetin-5-O-glucoside	Flavanone glycoside	[M-H]-	3.17	0.003888
39	Eriodictyol	Flavanone	[M-H]-	4.18	0.327823
40	Dihydrokaempferol	Dihydroflavonol	[M-H]-	3.53	0.011014
41	Taxifolin	Dihydroflavonol	[M-H]-	2.99	0.010918
42	Diosmetin	Flavone	[M-H]-	5.69	0.005955
43	Cynaroside	Flavone glycoside	[M-H]-	2.72	0.027473
44	Scutellarin	Flavone glycoside	[M-H]-	2.73	0.018501
45	Chrysoeriol	Flavone	[M-H]-	5.69	0.005955

General Observation of Condition

As shown in Figure 5B, the body weights of mice in all groups showed an upward trend during the experiment. Compared with Week 0 (the start of the experiment), the body weights of the mice in Weeks 1, 2, and 3 all increased significantly ($p < 0.01$). In contrast, body weight in the model group and the various treatment groups increased slowly, with both the magnitude and rate of weight gain during the experimental period being lower than those in the control group; however,

these differences were not statistically significant. By recording the mice's food intake every week, we found that the remaining food intake in the control group was (92.11±2.65) g, while that in the other groups was (105.24±2.52) g. This indicates that ozone induced modeling significantly suppressed appetite and food intake in all groups; however, observations of fur color and activity levels showed no significant differences compared to the control group, suggesting that this method of ozone induced modeling has a minimal impact on the aging of the mice's external phenotype.

Experimental Results on Navigation and Spatial Exploration in a Water Maze

As shown in Figure 5(C, D) and Table 6, during the navigation phase, the latency times for both the control group and the treatment groups decreased significantly starting on the third day ($p < 0.01$), indicating that the mice began to form spatial memories after the first two days of training. In contrast, this effect did not appear in the model group until the fifth day, suggesting that ozone induced modeling impaired the mice's learning and memory abilities, which improved following drug administration ($p < 0.01$). As shown in Figure 5E and Table 7, compared with the control group, the number of platform crossings was significantly reduced in the model group and the low-dose total flavonoids group ($p < 0.01$, $p < 0.05$); Compared with the model group, the number of platform crossings was significantly increased in the positive control group, the pine pollen group, and the medium- and high-dose total flavonoid groups ($p < 0.05$, $p < 0.01$, $p < 0.05$, $p < 0.05$). Compared with the control group, the residence time of mice in the target quadrant was significantly reduced in the model group ($p < 0.01$); Compared with the model group, the positive control group, pine pollen group, and low-, medium-, and high-dose total flavonoid groups showed significantly prolonged residence time in the target quadrant ($p < 0.01$, $p < 0.05$, $p < 0.05$, $p < 0.05$, $p < 0.05$). Based on the latency and test results, ozone induced modeling significantly impaired spatial learning and memory in mice. Following drug administration, learning and memory abilities improved in all groups, with the pine pollen group showing the greatest improvement, suggesting that pine pollen exerts its antiaging effects through the synergistic action of multiple components.

Tab.6 Incubation Period Timeline for Mice (n=10)

Group	Incubation period（s）				
	Day1	Day2	Day3	Day4	Day5
Con	59.07±2.15	57.17±5.41	22.62±7.97**	8.34±4.87**	7.26±3.99**
Mod	59.29±1.39	56.84±5.66	55.60±7.24	50.78±10.34	32.34±7.11**
PG	59.39±1.92	58.55±4.48	31.40±8.27##	23.08±8.95##	10.56±3.78##
CPG	58.83±2.67	55.56±7.06	28.91±6.94##	25.11±8.76##	12.12±5.29##
LG	59.11±2.49	56.72±5.66	28.41±9.11##	23.21±9.65##	19.17±8.78##
MG	59.43±1.79	56.40±7.56	34.20±9.67##	23.50±8.71##	14.47±5.59##
HG	59.75±1.09	54.84±7.51	42.98±8.89	21.69±6.94##	17.58±6.54##

$^{*}p < 0.05$, $^{**}p < 0.01$ compared with the control group; $^{\#}p < 0.05$, $^{\#\#}p < 0.01$ compared with the model group

Tab.7 Test Results from the Water Maze Test Period (n=10)

Group	Number of passes	Time spent in the target quadrant（%）
Con	4.17±0.90	36.96±1.65
Mod	2.38±0.86**	29.60±8.53**
PG	3.29±0.88#	38.53±5.54##
CPG	3.75±0.66##	35.88±3.84#
LG	3.00±1.00*	36.31±2.57#
MG	3.43±0.90#	36.69±5.06#
HG	3.33±0.75#	35.07±3.82#

$^{*}p < 0.05$, $^{**}p < 0.01$ compared with the control group; $^{\#}p < 0.05$, $^{\#\#}p < 0.01$ compared with the model group

Determination of Oxidative Stress Related Markers in Serum

As shown in Figure 6A, compared with the control group, GSH activity was extremely significantly reduced in the model group and the low-dose total flavonoids group ($p < 0.01$), and significantly reduced in the positive control group and the medium-dose total flavonoids group ($p < 0.05$); Compared with the model group, GSH activity was significantly increased in the positive control group and the

medium-dose total flavonoids group ($p < 0.05$), and was extremely significantly increased in the pine pollen group and the high-dose total flavonoids group ($p < 0.01$). As shown in Figure 6B, compared with the blank group, SOD activity was extremely significantly reduced in the model group, positive control group, and low-, medium-, and high-dose total flavonoid groups ($p < 0.01$), and significantly reduced in the pine pollen group ($p < 0.05$); Compared with the model group, SOD activity was extremely significantly increased in the positive control group and the pine pollen group ($p < 0.01$), and significantly increased in the high-dose total flavonoids group ($p < 0.05$). As shown in Figure 6C, compared with the control group, T-AOC activity was significantly reduced in the model group ($p < 0.05$); Compared with the model group, T-AOC activity increased in all treatment groups, but the results did not show significant differences. As shown in Figure 6D, compared with the blank group, MDA levels in the model group were significantly elevated ($p < 0.05$); compared with the model group, MDA levels in the pine pollen group and the high-dose total flavonoids group were significantly reduced ($p < 0.05$).

Based on the comprehensive test results, we found that both the pine pollen group and all dose groups of the total flavonoid extract effectively enhanced antioxidant enzyme activity in mouse serum, reduced the levels of harmful free radicals, and alleviated oxidative stress damage induced by ozone exposure. The significant decrease in antioxidant enzyme activity and the significant increase in harmful free radical levels in the model group may be attributed to the direct inhalation of ozone by the mice, which participates in the respiratory chain oxidation cycle, leading to a marked increase in the production of harmful free radicals and the inhibition of antioxidant enzyme activity [31,41].

Measurement of Inflammatory Markers in Serum

Oxidative stress damage can harm cells and is likely to induce inflammation while promoting aging [42]. The “danger signals” generated by this damage activate key intracellular inflammatory pathways (such as the NF-κB pathway); activation of this pathway leads to the production of large amounts of pro-inflammatory cytokines, such as the key markers TNF-α and IL-6, thereby initiating the body’s inflammatory

response [43,44] and further promoting aging. As shown in Figure 6E, TNF-α levels in the serum of mice in the model group were elevated, but the results did not show a significant difference. Although the various treatment groups were able to reduce TNF-α levels, the results similarly did not show a significant difference. Figure 6F shows a similar trend for IL-6 levels. This may be due to the fact that the degree of oxidative stress damage induced by ozone was insufficient to activate inflammatory pathways, or that the ozone modeling period was relatively short [45].

H&E staining results of mouse brain and lung tissues

The CA1 region of the hippocampus is of significant physiological importance and is closely associated with higher order brain functions [46]. The CA1 region of the hippocampus is responsible for learning, memory, and emotional regulation, and is closely linked to age related diseases such as Alzheimer's disease, epilepsy, and depression [47,48]. Therefore, observing pathological changes in the CA1 region of the hippocampus in mice is crucial in this study. As shown in Figure 7A, neurons in the hippocampal CA1 region of the blank control group were arranged in an orderly manner and exhibited intact morphology; in the model group, cells were scattered and sparse, with some showing atrophic morphology Figure 7B; in the positive drug control group and the pine pollen treatment group, neuronal morphology was significantly restored, and cell arrangement was relatively orderly Figure 7(C, D); the low-dose total flavonoids group did not significantly improve the number of neurons, and their arrangement remained relatively disorganized Figure 7E; compared with the model group, the medium- and high-dose total flavonoids groups significantly improved neuronal morphology, with a more orderly arrangement of cells Figure 7(F, G).

Since the ozone induced model involves direct inhalation of ozone into the lung tissue of mice, its effects on lung tissue are most pronounced [49,50]. We collected lung tissue from mice in each group, prepared sections, and examined them after staining. As shown in Figure 7A, the alveolar walls in the control group were thin, with good alveolar elasticity and expansion; there was no exudate, hemorrhage, or neutrophilic inflammatory infiltration. In contrast, the model group exhibited alveolar fusion,

significant structural damage, extensive neutrophil aggregation around the alveoli, severe inflammatory infiltration, and thickened alveolar walls Figure 7B; Compared with the model group, the alveolar structure in the positive control and pine pollen groups showed some recovery, with reduced alveolar wall thickening and improved inflammatory infiltration Figure 7(C, D); Compared with the model group, the low-, medium-, and high-dose total flavonoid groups significantly improved the alveolar structure in mice, with marked improvement in alveolar fusion and collapse, thinner alveolar walls, and restored elasticity; however, the state of inflammatory infiltration did not show significant improvement Figure 7(E, F, G).

Results of Nissl staining of mouse brain tissue

Nissl staining is a classic histological staining method that specifically visualizes neuronal cell bodies and is crucial for the diagnosis and assessment of age-related neurodegenerative diseases [51,52]. In this section, we continued to use the Nissl staining technique to stain the CA1 region of the hippocampus in mouse brain tissue for neuronal cell counting and observation. As shown in Figure 8(A, B) and Table 8, compared with the blank control group, the positive rate of neuronal cells was extremely significantly reduced in the model group ($p < 0.01$), and significantly reduced in the positive drug group and the low- and medium-dose total flavonoid groups ($p < 0.05$); compared with the model group, the positive rate of neuronal cells was extremely significantly higher in the cedar pollen group ($p < 0.01$), and significantly higher in the positive drug group and the medium- and high-dose total flavonoid groups ($p < 0.05$); all treatment groups alleviated ozone induced neuronal damage in the CA1 region of the mouse hippocampus, suggesting a protective effect against aging related neurodegenerative diseases. The results of Nissl staining and HE staining were mutually corroborative. All treatment groups effectively improved ozone induced neuronal damage in the CA1 region of the mouse hippocampus, suggesting they possess anti-aging effects and exert a protective role against age related neurodegenerative diseases.

Results of SA-β-gal staining of mouse brain tissue

Elevated SA-β-gal activity indicates that cells have entered an irreversible state

of proliferative arrest; it is an important marker of cellular senescence and is closely associated with age-related neurodegenerative diseases [51,53-55]. As shown in Figure 8(C, D) and Table 8, compared with the blank control group, SA-β-gal activity in the hippocampal CA1 region of brain tissue was extremely significantly elevated ($p < 0.01$) in the model group and the positive drug group, and significantly elevated ($p < 0.05$) in the pine pollen group and the low-dose total flavonoids group; Compared with the model group, SA-β-gal activity was extremely significantly reduced in the pine pollen group and the medium- and high-dose total flavonoid groups ($p < 0.01$), and significantly reduced in the low-dose total flavonoid group ($p < 0.05$). This indicates that all treatment groups exert an inhibitory effect on the age induced increase in SA-β-gal activity and can effectively prevent the onset and progression of age-related neurodegenerative diseases.

Tab.8 Results of Nissl and SA-β-gal staining of mouse brain tissue (n=3)

Group	Nissl Positive rate（%）	SA-β-gal Positive rate（%）
Con	0.82±0.0089	0.0467±0.0047
Mod	0.69±0.0087**	0.0637±0.0005**
PG	0.76±0.0262*#	0.0597±0.0019**
CPG	0.78±0.0394##	0.0540±0.0050*##
LG	0.75±0.0212*	0.0543±0.0019*#
MG	0.76±0.0334*#	0.0530±0.0022##
HG	0.77±0.0356#	0.0527±0.0037##

*$p < 0.05$, **$p < 0.01$ compared with the control group; #$p < 0.05$, ##$p < 0.01$ compared with the model group

Molecular Docking Results

Table 9 shows the binding energy results for 45 flavonoid compounds with Sirt1. Given that visualizing all 45 docking poses would be excessively cumbersome, we adopted a content-based ranking strategy to streamline the presentation. Specifically, the five compounds exhibiting the highest flavonoid content were selected for detailed visual analysis of their binding modes. The resulting docking conformations are

illustrated in Figure 9A. The binding energies of all these compounds are relatively low, indicating that all 45 compounds can spontaneously bind to Sirt1 and exert their effects.

Tab.9 Binding Energies of 45 Flavonoids to Sirt1

Compound	Binding energy (kcal/mol)	Compound	Binding energy (kcal/mol)
Luteolin-7-β-D-glucuronide	-9.941	Tamarixin	-7.498
Hyperoside	-7.589	Puerarin	-9.542
5-Methyl-7-methoxyisoflavone	-8.535	Sophoricoside	-10.77
Biochanin A	-9.112	Sophorobioside	-8.735
6-Methoxyflavone	-10.26	Diosmetol-7-glucoside	-10.7
Naringenin chalcone	-8.933	Apigenin-7-glucoside	-10.58
4',7-Di-O-methylnaringenin	-9.244	Thermopsoside	-10.77
Pinobanksin	-9.554	Phloretin	-8.681
Apiin	-9.202	(-)-Catechin	-7.048
Hydroxygenkwanin	-9.379	Afzelechin	-8.86
Naringenin	-9.299	Eriocitrin	-9.783
Norartocarpetin	-9.425	Poncirin	-9.31
6-Methoxyluteolin	-9.465	Didymin	-9.199
Apigenin-4'-O-glucoside	-10.69	Isosakuranetin	-9.387
Luteolin	-9.292	Hesperetin-5-O-glucoside	-9.638
Isorhamnetin	-8.869	Eriodictyol	-9.174
Quercetin-3-O-β-D-Glucuronide	-8.001	Dihydrokaempferol	-9.066
Quercetin-3-O-sophorose	-8.033	Taxifolin	-9.095
Narcissoside	-9.007	Diosmetin	-9.416
Isorhamnetin-3-O-glucoside	-9.03	Cynaroside	-7.53
Isorhamnetin-3-O-galactoside	-7.73	Scutellarin	-10.83
Myricetin	-9.597	Chrysoeriol	-9.434
Tiliroside	-10.52		

Expression Results for Related Genes

Sirt1 plays a critical role in the aging process, partly through its regulation of PGC1α, a key transcriptional coactivator that governs mitochondrial metabolism and oxidative stress responses [56]. During aging, PGC1α expression declines, leading to impaired mitochondrial antioxidant capacity and exacerbated oxidative damage. Conversely, pharmacological activation of the Sirt1-PGC1α axis upregulates PGC1α expression, enhances mitochondrial ROS scavenging, and attenuates oxidative stress, thereby contributing to the deceleration of age related pathological progression. As presented in Figure 9B, compared with the control group, the model group exhibited a marked reduction in both Sirt1 activity and PGC1α gene expression ($p < 0.01$). Notably, treatment with cedar pine pollen and its total flavonoids extracted via DES significantly reversed this trend, as evidenced by the substantial upregulation of these parameters relative to the model group ($p < 0.01$). These findings suggest that the observed antiaging effects of cedar pine pollen and its DES extracted flavonoids may be mediated, at least in part, through the attenuation of oxidative stress and the restoration of mitochondrial function related gene expression.

The mTOR signaling pathway is critically implicated in the aging process. Genetic or pharmacological inhibition of mTOR has been shown to mitigate oxidative stress induced damage in brain tissue and extend lifespan in model organisms [57]. This pathway is subject to upstream regulation by Sirt1, suggesting a potential interplay between these two key longevity-associated factors in the modulation of cellular stress responses and aging [56]. As shown in Figure 9B, compared with the control group, mTOR protein expression was significantly upregulated in the brain tissue of aged model mice ($p < 0.01$), suggesting an age associated activation of mTOR signaling. In contrast, treatment with cedar pine pollen or its extracts significantly reversed this upregulation ($p < 0.01$). These data indicate that the antiaging effects of cedar pine pollen and its extracts may be, at least in part, attributable to the suppression of mTOR activity, potentially involving the coordinated modulation of both the Sirt1-PGC-1α and Sirt1-mTOR signaling axes.

Discussion

The symbolic association of the pine tree with longevity in ancient Chinese culture is well documented in historical pharmacopoeia. The Qianjin Yifang records that prolonged consumption of pine needles “lightens the body, boosts vital energy, restores white hair, and prolongs life”, while the Taiping Shenghui Fang similarly states that long term use “prevents aging, lightens the body, and suppresses hunger”. These ancient claims have prompted modern investigations, which have shown that pine pollen ameliorates D-galactose-induced cognitive decline in mice via enhanced antioxidant defense and reduced inflammation [58], attenuates mitochondrial DNA deletions in aged murine kidneys [59], and improves hypothalamic-pituitary-testicular axis function in aged rats [60]. Despite these encouraging findings, however, most studies have focused on crude pollen preparations without identifying the specific bioactive constituents, and the overall evidence remains insufficiently robust to establish mechanistic clarity. Notably, cedar pollen, a locally abundant source in northwestern China traditionally used only for timber and landscaping has received little attention as a bioactive resource. Motivated by these considerations, the present study was undertaken to evaluate the antiaging potential of cedar pollen and its flavonoid-enriched fractions.

As noted above, flavonoids are widely recognized for their antiaging properties[9], leading us to hypothesize that the flavonoid constituents of cedar pollen are primarily responsible for its observed bioactivity. Following optimization of the DES based extraction protocol, the total flavonoid content and purity of cedar pollen extract increased by 3.42-fold and 8.12-fold, respectively, confirming that the established method is both stable and efficient for flavonoid enrichment. Given that conventional content determination methods are insufficient for comprehensive component profiling, we employed non-targeted metabolomics to characterize the chemical composition of the extract, and subsequently identified 45 candidate compounds via quantitative flavonoid analysis. These results provide a preliminary molecular basis for understanding the antiaging activity of the cedar pollen extract. Aging profoundly affects the central nervous system, predisposing elderly individuals to cognitive decline and neurodegenerative disorders such as Alzheimer's disease [61,62], which are

characterized by progressive memory impairment and loss of self-care ability. The Morris water maze test is a well-established paradigm for evaluating spatial learning and memory in laboratory animals. In the present study, treatment with cedar pollen and its total flavonoid extract significantly improved learning and memory performance in aged mice, accompanied by amelioration of neuronal damage. These behavioral and histopathological findings further corroborate the antiaging potential of cedar pollen and its flavonoid enriched fractions.

In recent years, accumulating evidence has established that Sirt1 serves as a pivotal regulator of multiple aging related signaling pathways [63-65]. However, direct associations between complex phytochemical constituents, their biological functions, and specific pathway modulations remain challenging to establish through conventional approaches. To address this gap, we performed molecular docking of the 45 identified flavonoid compounds against the Sirt1 protein, and the results demonstrated that all tested compounds exhibited effective binding affinity. Furthermore, qPCR analysis revealed that treatment with cedar pollen and its total flavonoid extract significantly upregulated the expression of Sirt1 and PGC-1α while downregulating mTOR expression, suggesting that the anti-aging effects are mediated, at least in part, through modulation of the Sirt1-PGC1α and Sirt-mTOR signaling axes. Collectively, the integration of non-targeted metabolomic profiling with quantitative flavonoid analysis validates the efficacy of the optimized DES based extraction protocol for cedar pollen flavonoids. This strategy enables targeted identification and quantitation of bioactive compounds from a complex phytochemical matrix, thereby circumventing the inefficiency inherent in untargeted screening approaches and contributing to reduced experimental costs. Nevertheless, we acknowledge that the current preliminary identification warrants further validation using more precise analytical techniques, such as high resolution mass spectrometry, for unequivocal structural elucidation. In parallel, future in vitro mechanistic studies are essential to establish direct causal relationships between specific chemical entities and their observed bioactivities, ultimately advancing our understanding of the molecular basis underlying the antiaging effects of cedar pollen flavonoids.

Materials and Methods

Reagents and Instruments

AE260 0.1 mg Electronic Balance (Mettler-Toledo Switzerland); CP225D 1 μg Electronic Balance (Sartorius Germany); UV-1800 UV-Vis Spectrophotometer (Shimadzu Japan); TD5A Centrifuge (Hunan Kaida Scientific Instrument Co., Ltd.); HWCL-3 Heat Collecting Constant Temperature Magnetic Stirring Bath (Zhengzhou Great Wall Science, Industry & Trade Co., Ltd.); Nicolet IS5 Fourier Transform Infrared Spectrometer (Shanghai Lijin Scientific Instruments Co., Ltd.); SU8100 Scanning Electron Microscope (Hitachi Ltd., Japan); Glass Chromatography Columns; Thermo Scientific Multiskan FC Microplate Reader (Thermo Fisher Scientific China Co., Ltd.); 5424R Refrigerated Centrifuge, U410 Ultra Low Temperature Freezer (Eppendorf AG, Germany); Animal Behavior Video Analysis System (Shanghai Jiliang Software Technology Co., Ltd.); Ultra high performance liquid chromatography (ExionLC™ AD) and tandem mass spectrometry (MS/MS) (QTRAP® 6500+); MU-G02-0448 Constant Temperature Metal Mixer (Hangzhou Meio Instruments Co., Ltd.); MS105DM 0.001 mg electronic balance (Mettler Toledo Instruments Co., Ltd.); CentriVap centrifugal concentrator (LABCONCO, Inc., USA); VORTEX-5 vortex mixer (Haimen Qilin Bell Instrument Manufacturing Co., Ltd.); KQ5200E ultrasonic cleaner (Kunshan Ultrasonic Instrument Co., Ltd.); MX-S Series Vortex Oscillator (Sirotek, Inc., USA); M10K Micro Mini Centrifuge (Shanghai Chengke Company); Aurora-900 Ultra Microvolume Spectrophotometer (Shanghai Chengke Company); T100 Thermal Cycler Gradient PCR System (Bio-Rad, Inc., USA); StepOne Plus Real-Time Quantitative PCR System (Thermo, USA).

Pollen of *Cedrus deodara* (Roxb.) G. Don was collected from two distinct locations in Gansu Province, China. The Tianshui Forestry Farm and the urban area of Lanzhou. Morphological characteristics of the pollen grains were examined by microscopy. Prior to extraction, the collected pollen was manually cleaned to remove extraneous materials (e.g., twigs and leaf fragments), thoroughly dried, and subjected to mechanical disruption to facilitate cell wall breakage. The processed pollen was

then stored in sealed containers under cool, dry conditions until further use.

Choline chloride (Lot No.: C17834062, purity 98%), citric acid (Lot No.: C17200650, purity≥99.5%), both manufactured by Shandong Keyuan Biochemical Co., Ltd.; lactic acid (Lot No.: 20250331, purity 90%), manufactured by Tianjin Kemio Chemical Reagents Co., Ltd.; glycerol (Lot No.: 20240808, purity≥99%), manufactured by Tianjin Fuyu Fine Chemical Co., Ltd.; 1,3-butanediol (Lot No.: KS369738, purity 99%) and 1,2-propanediol (Lot No.: KS373308, purity 99%), both manufactured by Shanghai Yuanye Biotechnology Co., Ltd.; urea (Lot No.: 202050501, purity 99%), manufactured by Yantai Shuangshuang Chemical Co., Ltd.; Rutin (Lot No.: PS012233, purity 99.8%), manufactured by Chengdu Pusi Biotechnology Co., Ltd.; Methanol (Lot No.: 20250701, analytical grade purity) and ethanol (Lot No.: 20230806, analytical grade purity), purchased from Tianjin Baishi Chemical Co., Ltd.; Sodium nitrite (Lot No.: 20180110), Ferrous sulfate (Lot No.: 20181130), and Salicylic acid (Lot No.: 20161025), purchased from Tianjin Kemio Chemical Reagents Co., Ltd.; Aluminum nitrate (Lot No.: 2023101601) and Sodium hydroxide (Lot No.: 20250602), purchased from Tianjin Damao Chemical Reagents Co., Ltd.; Ascorbic acid (Lot No.: F20181016), purchased from Sinopharm Chemical Reagents Co., Ltd.; 30% Hydrogen peroxide (Lot No.: 20180126), purchased from Chengdu Jinshan Chemical Reagents Co., Ltd.; 1,1-diphenyl-2-trinitrophenylhydrazine (DPPH) (Lot No.: C18060284), 2,2-azobenzene-di (3-ethylbenzothiazole-6-sulfonic acid) diammonium salt (ABTS) (Lot No.: C18271775), purchased from Shanghai McLean Biochemical Technology Co., Ltd.; D101, AB-8, DM-130, ADS-17, NKA-9, HPD-826 resins, purchased from Beijing Huideyi Technology Co., Ltd.; Formic acid (Lot No.: 695076-100ML, Aladdin Reagents Co., Ltd.); Acetonitrile (Lot No.: 5011403, Shanghai Xingke Reagents Co., Ltd.); Chromatographic grade methanol (Merck).; Vitamin C (Lot No.: 20200309, Tianjin Kemio Chemical Reagent Co., Ltd.); Saline solution (Lot No.: N25030705, Sichuan Kelun Pharmaceutical Co., Ltd.); Universal neutral tissue fixative (Lot No.: G1101-500ML, Wuhan Seville Biotechnology Co., Ltd.); MDA assay kit (Lot No.: 20260421), Reduced glutathione (GSH) assay kit (Lot No.:

20260420), Superoxide Dismutase (SOD) Assay Kit (Lot No.: 20260420), Total Antioxidant Capacity (T-AOC) Assay Kit (Lot No.: 20260507), all purchased from Nanjing Jiancheng Biotechnology Co., Ltd.; Mouse Tumor necrosis factor-α (TNF-α) ELISA Kit (Lot No.: RRDC2602003) and Mouse Interleukin-6 (IL-6) ELISA Kit (Lot No.: RRDC260202), both purchased from Wuhan Seville Biotechnology Co., Ltd.; Avertin Animal Anesthetic (Lot No.: K017422), Keckler (Guangzhou) Biomedical Co., Ltd; Total RNA Kit II (Lot No.: R6934010000K26X047), Omega Bio-Tek, Inc., USA; Evo M-MLV Reverse Transcription Kit (Lot No.: A7A1187), 2× qPCR Master Mix (SYBR Green) (Lot No.: A7A2331), ROX Reference Dye (Lot No.: A4A3163), Aicrui Biotechnology Engineering Co., Ltd.

Animal Husbandry and Medication Administration

A total of 70 SPF grade C57BL/6 mice (aged 6-8 weeks) were purchased from the Laboratory Animal Center of the Lanzhou Veterinary Research Institute, Chinese Academy of Agricultural Sciences. Production license number: SCXK (Gan) 2020-0002; animal qualification certificate number: 0002821. Animal Husbandry at the Lanzhou Institute for Food and Drug Inspection and Testing. SPF grade housing conditions: temperature (23±2) °C, humidity (50±5)%, Operating License No.: SYXK (Gan) 2019-0001. A 12-hour light/12-hour dark cycle was maintained. The experimental protocol was approved by the Laboratory Animal Ethics Review Committee of the Lanzhou Institute for Food and Drug Control, Gansu Province, and was conducted in strict accordance with relevant regulations. Ethics Review Approval No.: 2026-002.

A total of 70 C57BL/6 mice were acclimatized for 5 days. Ten mice were randomly selected to serve as the blank control group (Con). The remaining mice, with the exception of the model group (Mod), were first administered the drug via gavage daily between 8:00 and 9:00 a.m. for 14 days. Subsequently, they were placed in an ozone chamber together with the mice in the model group to induce the model, at an ozone concentration of (2.0±0.5) ppm, for 1 hour per day. Based on the dosing concentrations from the research group's previous experiments [39], the treatment groups were divided into a positive control group (Vc group) (PG), 200 mg/kg; a

cedar pollen group (CPG), 1.25 g/kg; low (LG), medium (MG), and high (HG) total flavonoid dose groups at (50, 100, 200) mg/kg, respectively. After 14 days of dosing and model induction, model induction was suspended for the following week, while oral administration continued daily at the same time. The water maze experiment began at 9:00 a.m. each day and lasted for a total of 6 days. The total experimental cycle lasted 21 days; see Figure 5A for the specific experimental protocol. During the experiment, mice in all groups had free access to food and water. Body weight was measured every 7 days, and changes in body weight were observed and recorded.

A Study on Methods for Determining Total Flavonoid Content

Preparation of the Test Solution

Accurately weigh 0.50 g of cell-disrupted cedar pollen and add it to a prepared DES mixture (HBA : HBD molar ratio of 1:2, 20% water content) at a solid-to-liquid ratio of 1:20 (g : mL). Heat the mixture on a magnetic stirrer for 15 minutes at a stirring speed of 500 rpm and a temperature of 70 °C. After the reaction, transfer the solution to a 25 mL volumetric flask in small portions using methanol, dilute to volume, filter through a 0.45 μm microporous membrane, and set aside.

Preparation of the Reference Solution and Evaluation of the Linear Relationship

Accurately weigh 6.14 mg of rutin, dissolve it in methanol, and dilute to volume in a 25 mL volumetric flask to prepare a rutin reference solution. Accurately pipette 0.5, 1, 1.5, 2, 2.5, and 3 mL of this solution into separate 10 mL volumetric flasks, dilute to volume, and set aside as solutions of various concentration gradients. For the reaction, first add 1 mL of each solution, followed by 0.3 mL of 5% sodium nitrite solution; shake well and allow to react for 6 minutes. Next, add 0.3 mL of 10% aluminum nitrate solution; shake well and allow to react for 10 minutes. Finally, add 4 mL of 4% sodium hydroxide solution; shake well and allow to react for 10 minutes. Use the corresponding solvent reaction as a blank and measure the absorbance at 510 nm. Plot a regression equation with the corresponding concentration gradient (x) on the x-axis and the absorbance value (y) on the y-axis.

Methodological Analysis

Accurately pipette a rutin standard solution of a specified concentration and

perform six parallel determinations as outlined in section “2.3.2”. Record the absorbance values and calculate the relative standard deviation (RSD) to assess instrument precision. Weigh 0.500 g of cell-broken cedar pollen in six separate portions. Prepare six test solutions in parallel according to the method described in “2.3.1”. Determine the content through six parallel measurements as specified in “2.3.2”, calculate the RSD, and obtain the method's repeatability results. Take 1 mL of the test solution prepared in accordance with section “2.3.1”. Measure the absorbance values at 0 h, 2 h, 4 h, 6 h, 8 h, 10 h, and 24 h using the method described in section “2.3.2”. Calculate the RSD values and assess whether the sample remains stable over a 24 hour period. Accurately weigh six portions of cedar pollen with known total flavonoid content. Prepare test solutions following the method described in “2.3.1”. Add a reference solution of consistent concentration to each, measure the absorbance values according to the method outlined in “2.3.2”, and calculate the spiked recovery and RSD values.

Screening of Solvents for DES Hydrogen Bond Donors and Acceptors

Deep Eutectic Solvents (DES) are typically prepared by mixing hydrogen-bond acceptors (HBAs) and hydrogen-bond donors (HBDs) in specific ratios. Common HBAs include choline chloride, while common HBDs include amides, carboxylic acids, and polyols. In this study, choline chloride was selected as the HBA, and lactic acid, 1,3-butanediol, 1,2-propanediol, glycerol, citric acid, and urea were used as HBDs. The reaction was carried out under the conditions listed in Table 10 until all solutes were completely dissolved, resulting in a uniform, transparent liquid with a certain viscosity, thereby preparing various DES solvents.

Tab.10 Preparation and Screening of Different DESs (n=3)

Solvent Code	HBA-HBD	molar ratio	Reaction conditions
DES1	Choline chloride - Lactic acid	1:2	70 ℃ 500 r/min
DES2	Choline chloride - 1,3-butanediol		
DES3	Choline chloride -1,2-Propanediol		
DES4	Choline chloride - Glycerol		
DES5	Choline chloride - Citric Acid		
DES6	Choline chloride - Urea,		

An Examination of Factors Influencing DES Extraction

By screening hydrogen bond donors and acceptors in the DES extraction solvent, the HBA-HBD pairs were fixed in subsequent experiments, with a constant rotation speed of 500 r/min. Following the method for preparing test solutions described in Section “2.3.1”, the factors affecting the extraction of total flavonoids from cedar pollen were investigated: the HBA-HBD molar ratio (1:1, 1:2, 1:3, 2:1, 3:1), moisture content (20%, 30%, 40%, 50%, 60%), and liquid-to-solid ratio (5:1, 10:1, 20:1, 30:1, 40:1), extraction temperature (40 °C, 50 °C, 60 °C, 70 °C, 80 °C), and extraction time (10 min, 15 min, 20 min, 30 min, 40 min).

Response Surface Optimization Experiments for the DES Extraction Process

After screening and analysis, we ultimately selected the HBA-HBD molar ratio, extraction temperature, and extraction time as the factors for the response surface optimization experiments. The table of factors and levels is shown in Table 11, the Box-Behnken design and results are shown in Table 1, and the results of the analysis of variance are shown in Table 2.

Tab.11 Factors and Levels

Level	Factors		
	A	B/°C	C/min
-1	1:1	60	10
0	1:2	70	15
1	1:3	80	20

A Study on the In Vitro Antioxidant Activity of DES Total Flavonoid Extract

Flavonoids are effective at scavenging harmful free radicals. Following the methodology described in a previous study [17], the total flavonoid extract obtained using DES as a solvent was evaluated for its in vitro antioxidant activity.

Fourier Transform Infrared Spectroscopy (FTIR)

First, prepare a blank slide coated with potassium bromide. Then, place a drop of the sample solution from each group onto the blank potassium bromide slide. The prepared DES blank solvent, 75% ethanol extract, and DES total flavonoid extract

were each mixed with potassium bromide, allowed to air-dry, and then analyzed.

Scanning electron microscopy analysis

To further investigate the effects of different extraction solvents on the structure of cedar pollen grains, we examined the microstructure of the pollen powder before and after DES extraction using scanning electron microscopy (SEM). Dried samples were firmly attached to conductive carbon coated double sided adhesive tape and placed on the sample stage of an ion sputtering system for gold sputtering for approximately 30 seconds. Subsequently, the samples were observed under the electron microscope, and images were captured for analysis.

Recycling of DES

Macroporous adsorption resins were selected to recover the DES extract for use in subsequent experimental studies. The adsorption and desorption rates were calculated separately to determine the optimal recovery efficiency.

$$\text{Adsorption rate} = (C_0V_1\text{-}C_1V_1)/C_0V_1 \times 100\%$$

$$\text{Desorption rate} = (C_2V_2)/(C_0V_1\text{-}C_1V_1) \times 100\%$$

$$\text{Recovery rate} = (C_2V_2/C_0V_1) \times 100\%$$

Calculation of Total Flavonoid Purity, let the concentration of the test solution be C. Dry an empty dish to constant weight and record its mass as m_0. Accurately pipette V mL of the test solution into an evaporating dish that has been dried to constant weight. Evaporate the solution to dryness on a water bath, then place the dish in an oven at 105 °C until constant weight is reached (approximately 3 hours). Remove the dish, allow it to cool naturally in a desiccator, and record the mass of the dish and the dried residue as m_1. Formula for calculating purity：

$$\text{Purity} = (C \times V)/(m_1\text{-}\ m_0) \times 100\%$$

Note: C_0 is the concentration of the extraction solution prior to adsorption; C_1 is the concentration of the remaining unadsorbed extraction solution at adsorption equilibrium; C_2 is the concentration of the desorption solution at desorption equilibrium. V_1 is the volume of the sample solution, and V_2 is the volume of the desorption solution.

Selection of Adsorption Resins

First, we examined the adsorption rates of flavonoids in the DES extract using

different resins to evaluate their effectiveness in adsorbing active components. Resins with varying polarities were selected, including D101, AB-8, DM-130 [40], ADS-17, NKA-9, and HPD-826. Following the standard macroporous resin purification procedure, which involves first washing the macroporous resin with pure water to remove residual ethanol, then adding an equal volume of DES extract to the activated resin, the adsorption rate was measured after 8 hours of static adsorption. The properties of each resin are shown in Table 12.

Tab.12 Properties of Different Resins

Resin Type	Core Type (Polarity)	Frame structure	Key Features	Selection Criteria
D101	Nonpolar	Polystyrene-divinyl benzene copolymer	The surface lacks polar functional groups and exhibits strong hydrophobic interactions; it has a large pore size (100-150 Å) and a specific surface area of 400-500 m^2/g	Prioritizes the adsorption of nonpolar and weakly polar components, making it suitable for the removal of polar impurities from crude extracts
AB-8	Weakly polar	Polystyrene-divinyl benzene copolymer (containing a small amount of polar groups, such as hydroxyl groups or ether bonds)	Combines hydrophobic interactions with weak polar adsorption; pore size 130-150 Å, specific surface area 480-520 m^2/g	Suitable for medium- to weakly polar compounds; offers better separation selectivity than non-polar resins and reduces the adsorption of strongly hydrophobic impurities
DM-130	Weakly polar	Polystyrene-divinyl benzene copolymer (modified by the introduction of	Uniform pore size (80-120 Å), specific surface area of 500-600 m^2/g, and high	Suitable for the enrichment of active ingredients in high-concentration extracts; produces sharp elution peaks,

		weakly polar groups)	adsorption capacity; excellent acid and alkali resistance	facilitating subsequent UPLC quantification
ADS-17	Medium polarity	Acrylate copolymers	The surface contains polar functional groups such as ester and hydroxyl groups, which adsorb via hydrogen bonding and dipole interactions; pore size: 60-100 Å; specific surface area: 300-400 m^2/g	Suitable for moderately polar compounds; it adsorbs highly polar active ingredients more effectively than nonpolar resins.
NKA-9	Medium polarity	Acrylate copolymers	High content of polar groups (ester groups + hydroxyl groups), strong adsorption selectivity; pore size 90-120 Å, specific surface area 250-350 m^2/g	Suitable for the separation of moderately to highly polar components; can be used for the targeted enrichment of polar active ingredients
HPD-826	Medium polarity	Acrylate copolymers	Pore size: 100-140 Å; specific surface area: 450-550 m^2/g; fast adsorption and desorption rates; high mechanical strength; good reusability	Highly versatile, it can be used for the simultaneous enrichment of mixed active ingredients in extracts and is suitable for industrial-scale separation

880 Optimization of Resin Adsorption Volume

Select DM-130 resin that has undergone activation treatment. Weigh a specific amount of resin and add an extractant solution with a volume that is a multiple of the resin weight. The “multiple of volume” refers to the ratio of the extractant volume to the resin weight; for example, adding 3 mL of extractant to 3 g of resin constitutes a 1-fold volume, while adding 6 mL constitutes a 2-fold volume. Referring to traditional macroporous resin elution and adsorption tests, set up groups with 1x, 2x, 3x, 4x, and 5x volume ratios. Determine the adsorption rate after 8 hours of static adsorption.

Optimal Resin Adsorption time

DM-130 resin that has undergone activation treatment was selected. A specific weight of the resin was weighed, and an amount of DES extraction solution equal to twice the volume of the resin was added to it. Static adsorption was performed for 2, 4, 6, 8, and 24 hours, and the adsorption rate was measured.

Desorption of flavonoids from resin

Because the DES extract has a certain viscosity, it is not suitable for traditional dynamic loading methods; therefore, we considered using static adsorption. When desorbing the flavonoids adsorbed on the resin using a static desorption method, we selected anhydrous ethanol, methanol, 75% ethanol, 60% ethanol, and 50% ethanol as desorption solvents. The desorption efficiency was found to be, in descending order: anhydrous ethanol > methanol > 75% ethanol > 60% ethanol > 50% ethanol. However, after multiple rounds of static desorption until the eluent became colorless, the desorption rate was only 51.05%. Therefore, we considered washing the fully statically adsorbed resin with water to remove residual DES extraction solution from the surface, then loading it onto a column for dynamic desorption.

Detection of Off-Target Metabolites in DES Extracts

The thawed extract was thoroughly mixed using a vortex mixer. An aliquot of 500 μL was then transferred to a sterile vial and lyophilized. The dried residue was reconstituted with 500 μL of 70% aqueous methanol containing an internal standard (IS), vortex mixed for 15 min, and ultrasonicated in an ice water bath for 10 min. The resulting mixture was centrifuged at 4 °C and 12000 rpm for 3 min. The supernatant

was carefully collected, filtered through a 0.22 μm microporous membrane, and transferred into a sample vial insert for subsequent UPLC-MS/MS analysis.

UPLC-MS/MS analysis was conducted using an Agilent SB-C18 column (1.8 μm, 2.1 mm × 100 mm) at 40 °C, with a mobile phase comprising 0.1% formic acid in water (A) and 0.1% formic acid in acetonitrile (B). The gradient elution program was: 0-9 min (5% B), 9-10 min (5%-95% B), 10-11 min (95%-5% B), and 11-14 min (5% B), at a flow rate of 0.35 mL/min and an injection volume of 2 μL. Mass spectrometry was performed on a triple quadrupole instrument with an ESI source operating in both polarities under the following conditions: source temperature 500 °C; ion spray voltage ±5500 V/−4500 V; GS1, GS2, and CUR at 50, 60, and 25 psi, respectively; and CID gas at high. MRM acquisition was employed with nitrogen as the collision gas (medium setting), and the DP and CE values were optimized for each transition, with MRM ion pairs monitored in time-segmented windows based on metabolite retention times.

Quantitative Metabolic Analysis of Flavonoids in DES Extracts

The frozen sample was removed from ultra-low-temperature storage (-80 °C) and thawed on ice. After thorough vortex mixing, a 50 μL aliquot was transferred to a centrifuge tube and mixed with 500 μL of 70% aqueous methanol containing an internal standard (IS), yielding a final IS concentration of 0.4 mg/L. The mixture was sonicated for 30 min and then centrifuged at 4 °C and 12000 rpm for 5 min. The supernatant was carefully aspirated, filtered through a 0.22 μm syringe filter, and transferred into an autosampler vial for subsequent LC-MS/MS analysis.

Chromatographic separation was performed on a Waters ACQUITY UPLC HSS T3 C18 column (1.8 μm, 100 mm × 2.1 mm) maintained at 40 °C. The mobile phase consisted of (A) ultrapure water containing 0.05% (v/v) formic acid and (B) acetonitrile containing 0.05% (v/v) formic acid. The gradient elution program was conducted at a flow rate of 0.35 mL/min as follows: 0-1 min, (90% B); 1-9 min, (80% B); 9-12.5 min, (70% B); 12.5-13.5 min, (95% B); 13.5-13.6 min, (95% B); 13.6-16 min, (90% B). The injection volume was 2 μL. Mass spectrometric detection was carried out on a Q-Trap 6500+ mass spectrometer equipped with an electrospray

ionization (ESI) source operating in both positive- and negative-ion modes. The ion source parameters were set as follows: source temperature, 550 °C; ion spray voltage, +5500 V (positive mode) and -4500 V (negative mode); and curtain gas (CUR), 35 psi. Data acquisition was performed in multiple reaction monitoring (MRM) mode, with the declustering potential (DP) and collision energy (CE) individually optimized for each ion transition.

A series of standard working solutions were prepared at concentrations of 0.5, 1, 5, 10, 20, 50, 100, 200, 500, 1000, 2000, 5000, 10000, and 20000 nmol/L. Each standard solution was analyzed under the same LC-MS/MS conditions, and the corresponding chromatographic peak areas for both the target analytes and the internal standard were recorded. Calibration curves were constructed by plotting the peak area ratio of each analyte to the internal standard (y-axis) against the nominal concentration of the analyte (x-axis), using a weighted (1/x) linear regression model.

The concentration of each analyte in the sample was determined by interpolating the measured peak area ratio of the analyte to the internal standard into the corresponding calibration curve linear equation. The flavonoid content in the original sample was then calculated according to the following equation:

$$\text{Flavonoid content (μmol/L)}=\frac{C\times V_1}{10^6\times V_2}$$

where C is the concentration (nmol/L) of the analyte derived from the calibration curve, V_1 is the volume of extraction solvent (μL), and V_2 is the volume of the sample aliquot (mL). The factor 10^6 is used for unit conversion from nmol/L to μmol/L and from μL to L.

Observation of the general condition of mice

The general physical condition of the animals in each group was assessed daily throughout the experimental period. Parameters monitored included mental status, spontaneous locomotor activity, coat appearance (color and texture), as well as food and water consumption. Body weight was recorded weekly at a fixed time point to minimize circadian variation.

Morris Water Maze Experiment

The Morris water maze test was conducted starting on day 15. All mice underwent a 5 day training phase, followed by a probe trial on day 6. During the behavioral testing period, model induction was temporarily suspended, while drug administration continued as scheduled. Place navigation test: On the first training day, each mouse was allowed to swim freely in the water maze for 30 s to acclimate to the environment, and was then placed on the submerged platform for 10-20 s for familiarization. Subsequently, mice were released into the water facing the pool wall from each of the four quadrants, one at a time. The time taken to locate the platform (escape latency) was recorded. This procedure was repeated daily for 5 consecutive days. If a mouse failed to find the platform within 60 s, the escape latency was recorded as 60 s, and the animal was manually guided to the platform and allowed to remain there for 20 s. Spatial probe test: 24 hours after the final training session, the platform was removed from the pool. Each mouse was placed into the water from the quadrant opposite to the original platform quadrant (i.e., the target quadrant), and its swimming path was recorded for 60 s. The time spent in the target quadrant and the number of platform site crossings were analyzed as measures of spatial memory retention.

Sample Collection and Preparation of Mouse Serum

At the conclusion of the experimental period, all mice were fasted for 12 h with free access to water prior to tissue collection. Following body weight measurement, the animals were anesthetized, and blood was collected via retro orbital plexus puncture. The blood samples were allowed to clot at room temperature, and serum was separated by centrifugation at 4 °C and 3000 rpm for 10 min. The resulting supernatant was carefully collected, aliquoted, and stored at -80 °C until further analysis. After blood collection, the mice were rapidly euthanized by cervical dislocation. The brain and lungs were immediately excised on an ice cold plate. For histological evaluation, brain and lung tissues from three mice per group were fixed in 4% paraformaldehyde for subsequent hematoxylin and eosin (H&E) staining and microscopic examination. The remaining brain and lung tissues from the other animals were rinsed with normal saline to remove residual blood, blotted dry with

filter paper, weighed, placed in cryogenic vials, and stored at -80 °C for biochemical analyses.

Assessment of Relevant Markers in Mouse Serum

Prior to the experiment, serum was diluted with saline in a specific ratio according to the relevant kit instructions. Following the kit instructions, the activities of SOD, GSH, and T-AOC, as well as the levels of MDA, TNF-α, and IL-6, were measured in the serum samples from each group of mice.

H&E staining

Brain and lung tissues were randomly collected from three mice in each group. After fixation in a 10% formaldehyde solution, the tissues were trimmed and rinsed prior to the experiment, then dehydrated using xylene and a gradient of ethanol, embedded in paraffin, and sectioned into coronal sections (3-5 μm thick). Routine HE staining was performed, followed by re-dehydration to transparency. After brief air drying, the sections were mounted with neutral resin and examined under a microscope.

Nissl staining of brain tissue

Brain tissue was randomly collected from three mice in each group and fixed in 4% paraformaldehyde for at least 24 hours. Prior to the experiment, the tissue was subjected to stepwise dehydration in a dehydrator, followed by embedding and sectioning. The sections were stained using the Nissl method, and the extent of neuronal damage was assessed by observing the deep staining of cell nuclei, the shrinkage of Nissl bodies, and tissue vacuolization.

SA-β-gal staining

Brain tissue was randomly collected from three mice in each group, frozen in an ultra low temperature freezer, and then sectioned. Prior to the experiment, the frozen sections stored at -20 °C were removed and allowed to thaw briefly at room temperature. The sections were gently washed with PBS, and a sufficient volume of staining fixative was added to ensure complete coverage of the tissue; they were fixed at room temperature for at least 15 min. Remove the fixative, then wash the sections three times with PBS, allowing at least 5 minutes between each wash. Use a

histochemical pen or hydrophobic pen to draw a circle around the tissue to prevent subsequent incubation solutions from flowing away. Add a sufficient volume of the staining working solution to the tissue and incubate overnight at 37 °C (in a non-CO_2 incubator) in the dark. After washing with PBS, observe under a microscope.

Molecular Docking

We performed molecular docking of Sirt1, a critical regulator of the Sirt1-mTOR signaling axis. The 3D structure of the Sirt1 receptor was obtained from the RCSB Protein Data Bank (PDB; https://www.rcsb.org/), and a set of 45 flavonoid compounds was selected as small molecule ligands, with their native structures retrieved from the PubChem database (https://pubchem.ncbi.nlm.nih.gov/). Prior to docking, the receptor protein was preprocessed as follows: crystallographic water molecules, buffer components, and heteroatoms were removed; backbone discontinuities were identified and repaired via homology modeling using Modeller to fill missing residues; and amino acid residue nomenclature was standardized according to PDB conventions. Protonation states were assigned by adding hydrogen atoms at a physiological pH of 7.4, and the hydrogen-bonding network was subsequently optimized using PropKa to predict the most favorable protonation equilibria. For ligand preparation, the lowest energy conformations of the two dimensional ligand structures were generated using OpenBabel, followed by energy minimization with a 500 step conjugate gradient algorithm employing the MMFF94s force field, which was validated as optimal in preliminary tests. Gasteiger partial charges were then assigned to satisfy the input requirements of AutoDock Vina, and the final ligand files were converted to PDBQT format while retaining rotatable bond information. The binding pocket was defined according to the availability of a co-crystallized ligand: for receptor structures containing a co-crystallized ligand, the grid box was centered on the ligand's center of mass with an 8.0 Å margin; for those without, the putative active site was predicted using DoGSiteScorer, and the grid box dimensions were adjusted to cover 90.0% of the predicted site, with sizes ranging from 20.0 to 100.0 Å depending on the protein size.

RT-qPCR

Total RNA was extracted from mouse brain tissue using Solv Reagent, mercaptoethanol, chloroform, and a total RNA extraction kit. The RNA concentration and purity were determined, cDNA was synthesized via reverse transcription, and the final Ct values were obtained using a two step PCR protocol. The data were analyzed using the $2^{-\triangle\triangle CT}$ method. The list of gene sequences used is shown in Table 13.

Tab. 13 List of forward and reverse used in the gene expression study

Genes	Forward	Reverse
Sirt1	TCGGCTACCGAGGTCCATA	ACAATCTGCCACAGCGTCAT
mTOR	CACAAGGAGATCCGCATGGA	GCGGATATCAGGGTCAGGAT
PGC1α	AACCCCTTCCAACCAGTGTG	TTCCGATTGGTCGCTACACC
GAPDH	TGTGTCCGTCGTGGATCTGA	TTGCTGTTGAAGTCGCAGGAG

Data analysis

Statistical analysis was performed using SPSS 25.0 software. Results are expressed as （$\bar{x}$±s）. Differences in body weight at each time point were analyzed using repeated measures analysis of variance (ANOVA). For comparisons of other data between groups, if the data followed a normal distribution, ANOVA was used; if the data followed a normal distribution and variances were homogeneous, pairwise comparisons were performed using the LSD test; if variances were not homogeneous, pairwise comparisons were performed using the Games-Howell test; If the data did not follow a normal distribution and variances were unequal, the independent-samples Kruskal-Wallis test was used. For all tests, a significance level of $p < 0.05$ was adopted, and $p < 0.01$ indicated a highly significant difference in the experimental results. Staining data were processed using ImageJ, with results expressed as （$\bar{x}$±s）. Data processing methods were the same as described above.

Abbreviations: ABTS, 2,2'-Azino-bis(3-ethylbenzothiazoline-6-sulfonic acid) Diammonium Salt; ANOVA, Analysis of Variance; CE, Collision Energy; DES, Deep Eutectic Solvent; DP, Declustering Potential; DPPH, 2,2-Diphenyl-1-Picrylhydrazyl; ESI, Electrospray Ionization; FTIR, Fourier Transform Infrared Spectroscopy; GAPDH, Glyceraldehyde-3-Phosphate Dehydrogenase;

GSH, Reduced Glutathione; H&E, Hematoxylin and Eosin; HBA, Hydrogen Bond Acceptor; HBD, Hydrogen Bond Donor; IC_{50}, Half Maximal Inhibitory Concentration; IL-6, Interleukin-6; LSD, Least Significant Difference; MDA, Malondialdehyde; MRM, Multiple Reaction Monitoring; mTOR, Mammalian Target of Rapamycin; NAD^+, Nicotinamide Adenine Dinucleotide; OH^-, Hydroxyl Radical; PBS, Phosphate-Buffered Saline; PDB, Protein Data Bank; PGC1α, Peroxisome Proliferator-Activated Receptor Gamma Coactivator 1-Alpha; RSD, Relative Standard Deviation; RT-qPCR, Reverse Transcription Quantitative PCR; SA-β-gal, Senescence-Associated β-Galactosidase; SEM, Scanning Electron Microscopy; SIRT1, Sirtuin 1; SOD, Superoxide Dismutase; SPF, Specific Pathogen Free; T-AOC, Total Antioxidant Capacity; TNF-α, Tumor Necrosis Factor-Alpha; UPLC-MS/MS, Ultra-Performance Liquid Chromatography-Tandem Mass Spectrometry.

Author contributions

Wanyu Li：Writing-original draft, Writing-review & editing, Visualization. **Guanjie Wu**：Methodology, Validation. **Mian Chen**：Investigation, Data curation. **Xingmeng Zhai:** Formal analysis, Validation. **Lei Kang:** Software, Methodology. **Guangmiao Gao**：Investigation, Resources. **Yawen Du:** Data curation, Formal analysis. **Yapeng Zhao:** Supervision. **Gongjian Zhu**：Conceptualization, Methodology, Supervision, Resources, Project administration. **Xiaofeng Shi**：Resources, Writing-review & editing, Funding acquisition.

Funding

Project of the 6th Lanzhou Talent Innovation and Entrepreneurship Competition (2023-01-02)

Conflict of interest

The authors declare that the research was conducted in the absence of any commercial or financial relationships that could be construed as a potential conflict of interest.

References

1. Partridge, L., Deelen, J., & Slagboom, P. E. (2018). Facing up to the global challenges of ageing. Nature, 561(7721), 45-56. https://doi.org/10.1038/s41586-018-0457-8

2.Gianfredi, V., Nucci, D., Pennisi, F., et al. (2025). Aging, longevity, and healthy aging: the public health approach. Aging Clinical and Experimental Research, 37(1), 125.

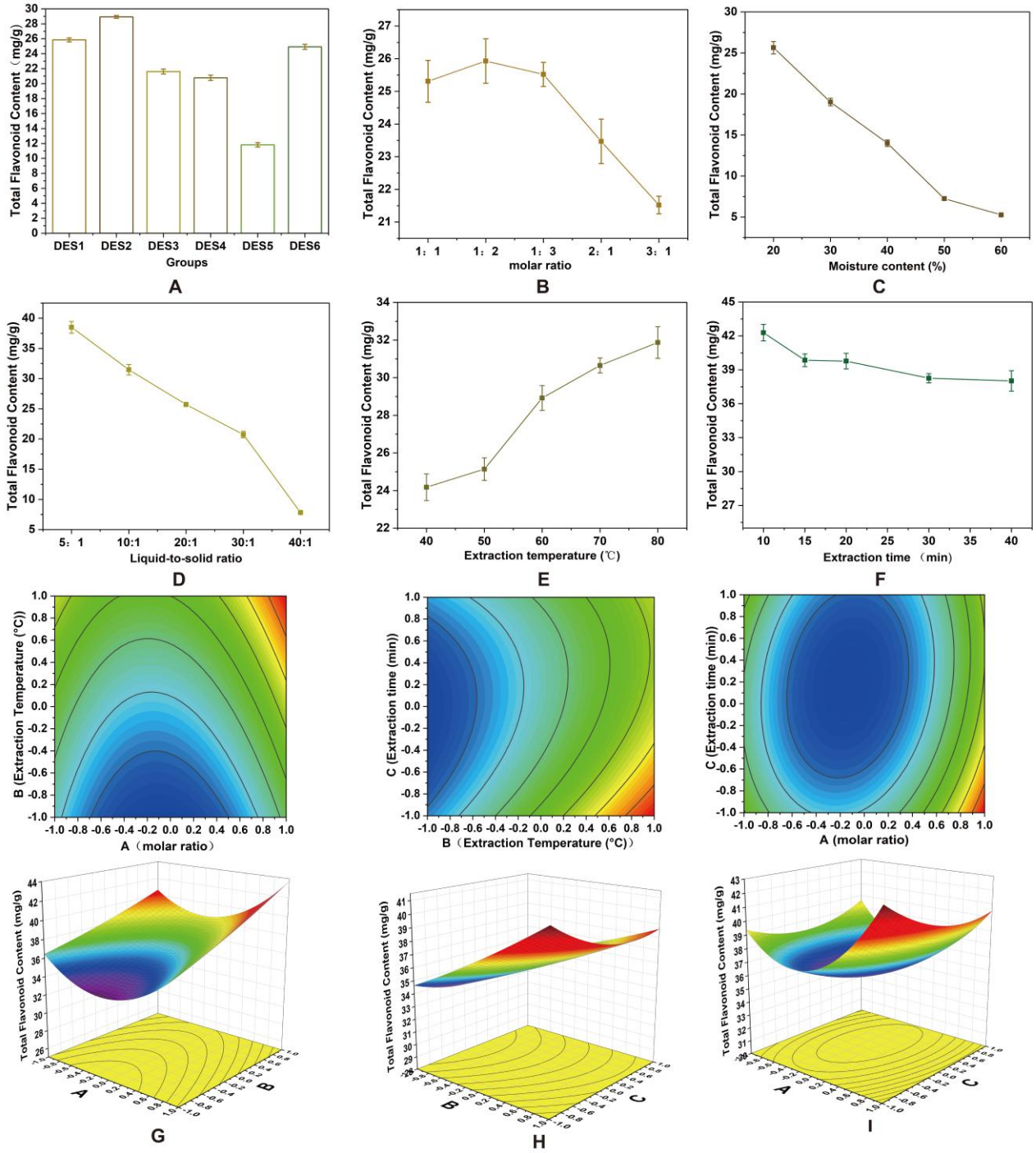
https://doi.org/10.1007/s40520-025-03021-8
3.Ma, Y., Erb, M. L., & Moore, D. J. (2025). Aging, cellular senescence and Parkinson's disease. Journal of Parkinson's Disease, 15(2), 239-254. https://doi.org/10.1177/1877718X251316552
4.Albarrati, A., & Gale, N. S. (2025). The aging lung: exploring multimorbidity patterns and their clinical implications: a narrative review. Current Issues in Molecular Biology, 47(7), 1-14. https://doi.org/10.3390/cimb47070561
5.Abo Qoura, L., Churov, A. V., Maltseva, O. N., et al. (2026). The aging interactome: from cellular dysregulation to therapeutic frontiers in age-related diseases. Biochimica et Biophysica Acta Molecular Basis of Disease, 1872(1), 168060. https://doi.org/10.1016/j.bbadis.2025.168060
6.Dong, R., Dong, R., Kan, J., et al. (2026). Insights into the therapeutic strategies for aging and aging-associated diseases. Signal Transduction and Targeted Therapy, 11(1), 202. https://doi.org/10.1038/s41392-026-02662-z
7.Zhou, Z. Y., Zhou, Z. Y., Duan, H. T., et al. (2026). Progress in anti-ageing drug research for age-related diseases: a review. Ageing Research Reviews, 114, 102982. https://doi.org/10.1016/j.arr.2025.102982
8.Lin, Y., Lin, Y., Altulea, A., et al. (2026). Effects of nutritional interventions on biomarkers of cellular senescence in humans: a systematic review. Ageing Research Reviews, 121, 103224. https://doi.org/10.1016/j.arr.2026.103224
9.Păcularu-Burada, B., Cîrîc, A. I., & Begea, M. (2024). Anti-aging effects of flavonoids from plant extracts. Foods, 13(15), 1-30. https://doi.org/10.3390/foods13152441
10.Fan, X., Fan, Z., Yang, Z., et al. (2022). Flavonoids-natural gifts to promote health and longevity. International Journal of Molecular Sciences, 23(4), 2176. https://doi.org/10.3390/ijms23042176
11.Niu, Y., Liao, J., Zhou, H., et al. (2022). Flavonoids from Lycium barbarum leaves exhibit anti-aging effects through the redox-modulation. Molecules, 27(15), 4952. https://doi.org/10.3390/molecules27154952
12.Gu, Y., Xue, F., Xiao, H., et al. (2022). Bamboo leaf flavonoids suppress oxidative stress-induced senescence of HaCaT cells and UVB-induced photoaging of mice through p38 MAPK and autophagy signaling. Nutrients, 14(4), 793. https://doi.org/10.3390/nu14040793
13.Wang, Z., Wang, W., Zhu, C., et al. (2022). Evaluation of antioxidative and neuroprotective activities of total flavonoids from sea buckthorn (Hippophae rhamnoides L.). Frontiers in Nutrition, 9, 861097. https://doi.org/10.3389/fnut.2022.861097
14.Si, Y., Li, Y., Gu, K., et al. (2024). Icariin ameliorates osteoporosis in ovariectomized rats by targeting Cullin 3/Nrf2/OH pathway for osteoclast inhibition. Biomedicine & Pharmacotherapy, 173, 116422. https://doi.org/10.1016/j.biopha.2024.116422
15.Liang, S. B., Liang, N., Bu, F. L., et al. (2020). The potential effects and use of Chinese herbal medicine pine pollen (Pinus pollen): a bibliometric analysis of pharmacological and clinical studies. World Journal of Traditional Chinese Medicine, 6(2), 163-170. https://doi.org/10.4103/wjtcm.wjtcm_4_20
16.Liu, Q., Sun, L., Ding, Y., et al. (2024). Chemical composition, health benefits, food processing effects and applications of Boletus: a review. Critical Reviews in Food Science and Nutrition, 64(29), 10812-10834. https://doi.org/10.1080/10408398.2023.2229426
17.Xin Anqi, Li Wanyu, Wang Mengfan, et al. (2025). Optimization of extraction process for total

flavonoids from Cedrus deodara pine pollen and evaluation of their anti-oxidant activity. Chinese Traditional Patent Medicine, 47(8), 2530-2534. https://doi.org/10.3969/j.issn.1001-1528.2025.08.007
18.Ling, J. K. U., & Hadinoto, K. (2022). Deep eutectic solvent as green solvent in extraction of biological macromolecules: a review. International Journal of Molecular Sciences, 23(6), 3381. https://doi.org/10.3390/ijms23063381
19.Zhang, Y., Liu, H., Hu, R., et al. (2025). Extraction of valuable metals from waste Li-ion batteries by deep eutectic solvent: experimental and mechanism analysis. AIChE Journal, 71(4):e18714. https://doi.org/10.1002/aic.18714
20.Altunay, N., & Tüzen, M. (2021). A simple and green ultrasound liquid-liquid microextraction method based on low viscous hydrophobic deep eutectic solvent for the preconcentration and separation of selenium in water and food samples prior to HG-AAS detection. Food Chemistry, 364, 130371. https://doi.org/10.1016/j.foodchem.2021.130371
21.Sun, J., Bao, W., Zhang, C., et al. (2024). Development of liquid phase microextraction-based deep eutectic solvent for the extraction and determination of toxic metal ions in herbal medicines. Toxin Reviews, 43(4), 505-512. https://doi.org/10.1080/15569543.2024.2369158
22.Afshar Mogaddam, M. R., Farajzadeh, M. A., Mohebbi, A., et al. (2020). Hollow fiber-liquid phase microextraction method based on a new deep eutectic solvent for extraction and derivatization of some phenolic compounds in beverage samples packed in plastics. Talanta, 216, 120986. https://doi.org/10.1016/j.talanta.2020.120986
23.Gamare, J. S., & Vats, B. G. (2023). A hydrophobic deep eutectic solvent for nuclear fuel cycle: extraction of actinides and dissolution of uranium oxide. European Journal of Inorganic Chemistry, 26, e202300441. https://doi.org/10.1002/ejic.202300441
24.Patil, S. M., Jayachandran, K., Sahu, M., et al. (2023). Efficient plutonium extraction and electrochemical insights in a hydrophobic deep eutectic solvent for radioactive waste management. Journal of the Electrochemical Society, 170(11), 113503. https://doi.org/10.1149/1945-7111/ad0adc
25.Fernandes, C., Melro, E., Magalhães, S., et al. (2021). New deep eutectic solvent assisted extraction of highly pure lignin from maritime pine sawdust (Pinus pinaster Ait.). International Journal of Biological Macromolecules, 177, 294-305. https://doi.org/10.1016/j.ijbiomac.2021.02.088
26.Sharma, M., & Dash, K. K. (2021). Deep eutectic solvent-based microwave-assisted extraction of phytochemical compounds from black jamun pulp. Journal of Food Process Engineering, 44(8), e13750. https://doi.org/10.1111/jfpe.13750
27.Zheng, B., Yuan, Y., Xiang, J., et al. (2021). Green extraction of phenolic compounds from foxtail millet bran by ultrasonic-assisted deep eutectic solvent extraction: optimization, comparison and bioactivities. LWT-Food Science and Technology, 154, 112740. https://doi.org/10.1016/j.lwt.2021.112740
28.Ge, Y., Ge, Y., He, C., et al. (2025). Simultaneous recovery of mannooligosaccharides and chlorogenic acids from spent coffee grounds: integration of enzymatic hydrolysis with natural deep eutectic solvent extraction. Journal of Agricultural and Food Chemistry, 73(51), 32577-32587. https://doi.org/10.1021/acs.jafc.5c11408
29.Silva-Palacios, A. (2022). ER stress in cardiac aging, a current view on the D-galactose model. Experimental Gerontology, 169, 111953. https://doi.org/10.1016/j.exger.2022.111953

30.Baeta-Corral, R., Castro-Fuentes, R., & Giménez-Llort, L. (2018). Sexual dimorphism in the behavioral responses and the immunoendocrine status in d-galactose-induced aging. The Journals of Gerontology: Series A, 73(9), 1147-1157. https://doi.org/10.1093/gerona/gly031
31.Feng, R., He, W., & Ochi, H. (2001). A new murine oxidative stress model associated with senescence. Mechanisms of Ageing and Development, 122(6), 547-559. https://doi.org/10.1016/s0047-6374(01)00232-9
32.Xing Haoyang, Hu Xinmin, Liu Honglian, et al. (2001). Study on DNA Oxidative Damage of O3 Aging Model in Mice. JWCUMS, 32(2), 229-231.
33.Pan, S. Y. (1994). Effects of ozone on exploratory behavior, passive avoidance responses, and M receptors and LPO in the brain of mice. Basic Medicine and Clinical Practice. Basic Medicine and Clinical Practice, 14(1), 75-76. https://doi.org/10.16352/j.issn.1001-6325.1994.01.043
34.Montoya-Estrada, A., García-Cortés, A. Y., Romo-Yañez, J., et al. (2024). The administration of resveratrol and vitamin C reduces oxidative stress in postmenopausal women-a pilot randomized clinical trial. Nutrients, 16(21), 3775. https://doi.org/10.3390/nu16213775
35.Başeğmez, M., Eryavuz, A., & Demirel, H. H. (2025). Effects of vitamin C supplementation on total antioxidant status, inflammation, and histopathological changes in aged rats. Journal of Biochemical and Molecular Toxicology, 39(6), e70324. https://doi.org/10.1002/jbt.70324
36.Chen, X., Chen, X., He, C., et al. (2024). Associations between dietary carotenoid and biological age acceleration: insights from NHANES 2009-2018. Biogerontology, 26(1), 24. https://doi.org/10.1007/s10522-024-10160-4
37.Ji, Z., Liu, G. H., & Qu, J. (2021). Mitochondrial sirtuins, metabolism, and aging. Journal of Genetics and Genomics, 49 (2022) 287e298. https://doi.org/10.1016/j.jgg.2021.11.005
38.Kennedy, B. K. (2021). Sirtuins and mTOR in aging pathways – the role of cell senescence. Free Radical Biology and Medicine, 165, 12. https://doi.org/10.1016/j.freeradbiomed.2020.12.273
39.Peng Tengteng, Wang Xin, Li Haiyan, et al. (2024). Effects of Paeonia rockii pollen on D-galactose aging model mice. Chinese Pharmacological Bulletin, 40(4), 730-739. https://doi.org/10.12360/CPB202309052
40.Zhang Min, Sun Huapeng, Huang Fan, et al. (2016). Purification of Total Flavonoid from Pinus massoniana Pollen with Macroporous Resin. Storage and Process, 16(5), 36-40. https://doi.org/10.3969/jissn.1009-6221.2016.05.008
41.Alexeeff, S. E., Litonjua, A. A., Wright, R. O., et al. (2008). Ozone exposure, antioxidant genes, and lung function in an elderly cohort: VA normative aging study. Occupational and Environmental Medicine, 65(11), 736-742. https://doi.org/10.1136/oem.2007.035253
42.Scarian, E., Viola, C., Dragoni, F., et al. (2024). New insights into oxidative stress and inflammatory response in neurodegenerative diseases. International Journal of Molecular Sciences, 25(5), 2698. https://doi.org/10.3390/ijms25052698
43.Taherkhani, S., Suzuki, K., & Castell, L. M. (2020). A short overview of changes in inflammatory cytokines and oxidative stress in response to physical activity and antioxidant supplementation. Antioxidants, 9(9), 886. https://doi.org/10.3390/antiox9090886
44.Ali, T., & Kim, M. O. (2015). Melatonin ameliorates amyloid beta-induced memory deficits, tau hyperphosphorylation and neurodegeneration via PI3/Akt/GSk3β pathway in the mouse hippocampus. Journal of Pineal Research, 59(1), 47-59. https://doi.org/10.1111/jpi.12238

45.Singh, A. S., Suresh, S., & Vellapandian, C. (2023). Ozone-induced neurotoxicity: in vitro and in vivo evidence. Ageing Research Reviews, 91, 102045. https://doi.org/10.1016/j.arr.2023.102045
46.Crown, L., Gray, D. T., Schimanski, L. A., et al. (2022). Aged rats exhibit altered behavior-induced oscillatory activity, place cell firing rates, and spatial information content in the CA1 region of the hippocampus. Journal of Neuroscience, 42(22), 4505-4516. https://doi.org/10.1523/JNEUROSCI.1855-21.2022
47.Mehder, R. H., Bennett, B. M., & Andrew, R. D. (2021). Age-related neuronal deterioration specifically within the dorsal CA1 region of the hippocampus in a mouse model of late onset Alzheimer's disease. Journal of Alzheimer's Disease, 79(4), 1547-1561. https://doi.org/10.3233/JAD-201024
48.Li, H., Ye, T., Liu, X., et al. (2023). The role of signaling crosstalk of microglia in hippocampus on progression of ageing and Alzheimer's disease. Journal of Pharmaceutical Analysis, 13(7), 788-805. https://doi.org/10.1016/j.jpha.2023.05.008
49.Sun Xiaoning, Su Deqi, Yang Haofeng, et al. (2024). Effects of acute exposure to ozone on lung tissue injury in rats. CARCINOGENESIS. TERATOGENESIS & MUTAGENESIS, 36(3), 219-223. https://doi.org/10.3969/j.issn.1004-616x.2024.03.008
50.Greve, H. J., Dunbar, A. L., Garza-Lombó, C., et al. (2022). The bidirectional lung brain-axis of amyloid-β pathology: ozone dysregulates the peri-plaque microenvironment. Brain, 146(3), 991-1005. https://doi.org/10.1093/brain/awac113
51.Faryadras, K., Golchoobian, R., Iranzadeh, S., et al. (2025). Promising neuroprotective potential of naringenin against trimethyltin-induced cognitive deficits and hippocampal neurodegeneration in rats. Frontiers in Neuroscience, 19, 1567236. https://doi.org/10.3389/fnins.2025.1567236
52.Niu, J., Li, C., Wu, H., et al. (2015). Propidium iodide (PI) stains Nissl bodies and may serve as a quick marker for total neuronal cell count. Acta Histochemica, 117(2), 182-187. https://doi.org/10.1016/j.acthis.2014.12.001
53.Tokmakov, A. A., & Sato, K. I. (2019). Activity and intracellular localization of senescence-associated β-galactosidase in aging Xenopus oocytes and eggs. Experimental Gerontology, 119, 157-167. https://doi.org/10.1016/j.exger.2019.02.002
54.Li, X., Qiu, W., Li, J., et al. (2020). First-generation species-selective chemical probes for fluorescence imaging of human senescence-associated β-galactosidase. Chemical Science, 11(28), 7292-7301. https://doi.org/10.1039/d0sc01234c
55.Račková, L., Kodríková, R., Nemčovič, M., et al. (2025). Exploring glycobiomarkers beyond senescence-associated β-galactosidase for studying aging in vitro. Biochimie, 239(Pt B), 218-235. https://doi.org/10.1016/j.biochi.2025.09.005
56.Chen, C., Zhou, M., Ge, Y., et al. (2020). SIRT1 and aging related signaling pathways. Mechanisms of Ageing and Development, 187, 111215. https://doi.org/10.1016/j.mad.2020.111215
57.Chen, E. B., Narayan, N., Rovira, I. I., et al. (2013). Increased mammalian lifespan and a segmental and tissue-specific slowing of aging after genetic reduction of mTOR expression. Cell Reports, 4(5), 913-920. https://doi.org/10.1016/j.celrep.2013.07.030
58.Mao, G. X., Zheng, L. D., Cao, Y. B., et al. (2012). Antiaging effect of pine pollen in human diploid fibroblasts and in a mouse model induced by D-galactose. Oxidative Medicine and

Cellular Longevity, 2012, 750963. https://doi.org/10.1155/2012/750963
59.Yu, Lu, & Shi, Chunxia. (2012). Effect of pine pollen on kidney mitochondria DNA deletion mutation in senile mice. China Journal of Chinese Materia Medica, 37(11), 1663-1666. https://doi.org/10.4268/cjcmm20121134
60.Niu Siyun, Pang Xiaojing, Gao Fulü, et al. (2006). The Regulatory Effects of Pine Pollen on the Hypothalamic-Pituitary-Testicular Axis in Rats with a Subacute D-Galactose-Induced Aging Model. Chinese Journal of Gerontology, (8), 1098-1099.
61.Jost, Z., & Kujach, S. (2025). Understanding cognitive decline in aging: mechanisms and mitigation strategies-a narrative review. Clinical Interventions in Aging, 20, 459-469. https://doi.org/10.2147/CIA.S510670
62.Abrous, D. N., Blin, N., Boraxbekk, C. J., et al. (2026). Hallmarks of healthy cognitive aging: inter-individual differences in aging trajectories. Ageing Research Reviews, 119, 103102. https://doi.org/10.1016/j.arr.2026.103102
63.Wen, S. Y., Ng, S. C., Chiu, Y. T., et al. (2024). Enhanced SIRT1 activity by galangin mitigates UVB-induced senescence in dermal fibroblasts via p53 acetylation regulation and activation. Journal of Agricultural and Food Chemistry, 72(42), 23286-23294. https://doi.org/10.1021/acs.jafc.4c05945
64.Sousa, C., & Mendes, A. F. (2022). Monoterpenes as sirtuin-1 activators: therapeutic potential in aging and related diseases. Biomolecules, 12(7), 921. https://doi.org/10.3390/biom12070921
65.Karolczak, K., Karolczak, K., Karolczak, K., et al. (2023). Estradiol as the trigger of sirtuin-1-dependent cell signaling with a potential utility in anti-aging therapies. International Journal of Molecular Sciences, 24(18), 13753. https://doi.org/10.3390/ijms241813753



13:

1322 Fig.1 Optimization of DES Extraction Conditions (n=3)

1323



A B

1324

1325

1326

1327

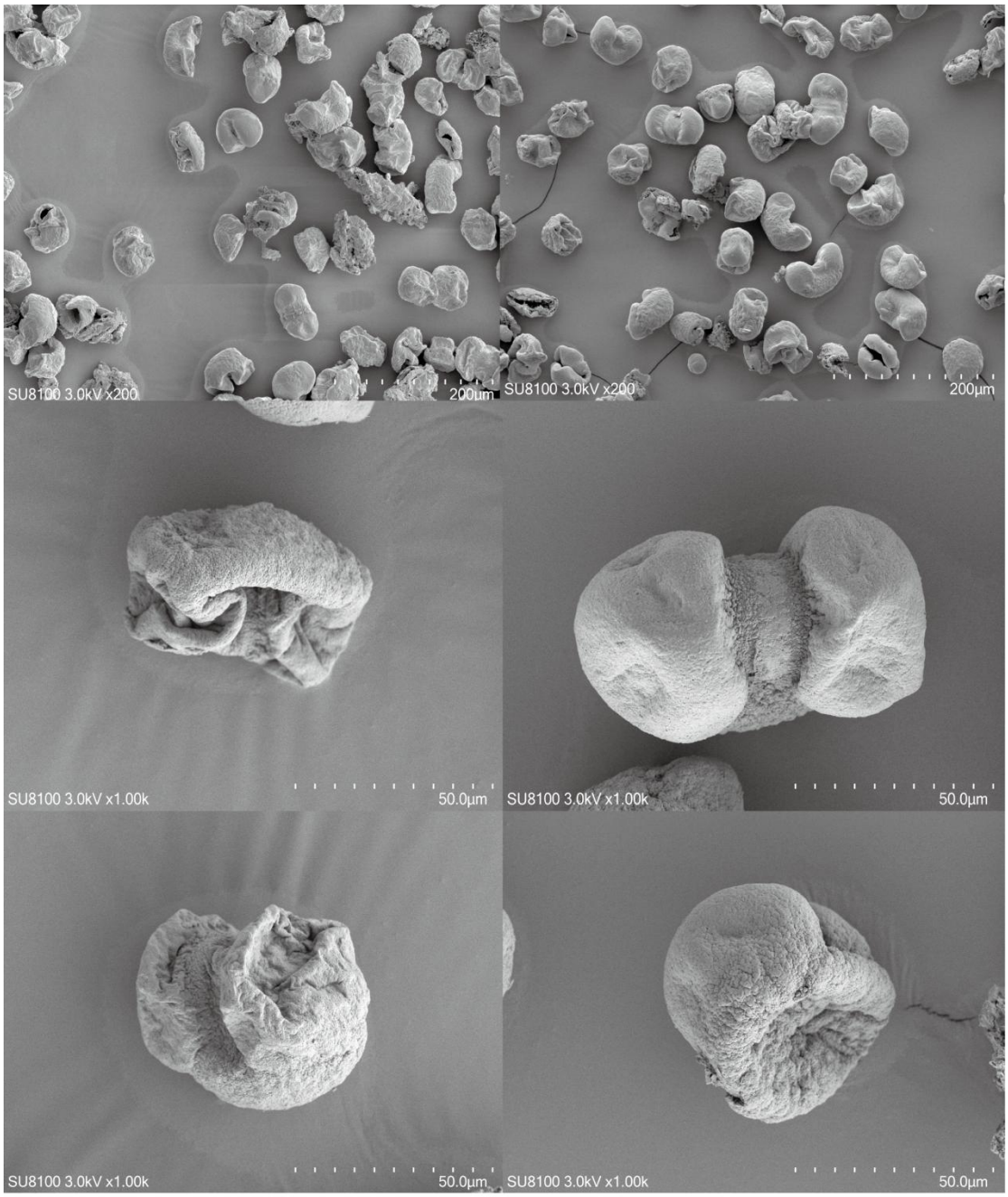


Fig.2 Scanning electron microscope images

(A) Uncracked pollen, (B) Cracked pollen, (C) Pollen extracted with 75% ethanol,

(D) Pollen extracted with DES

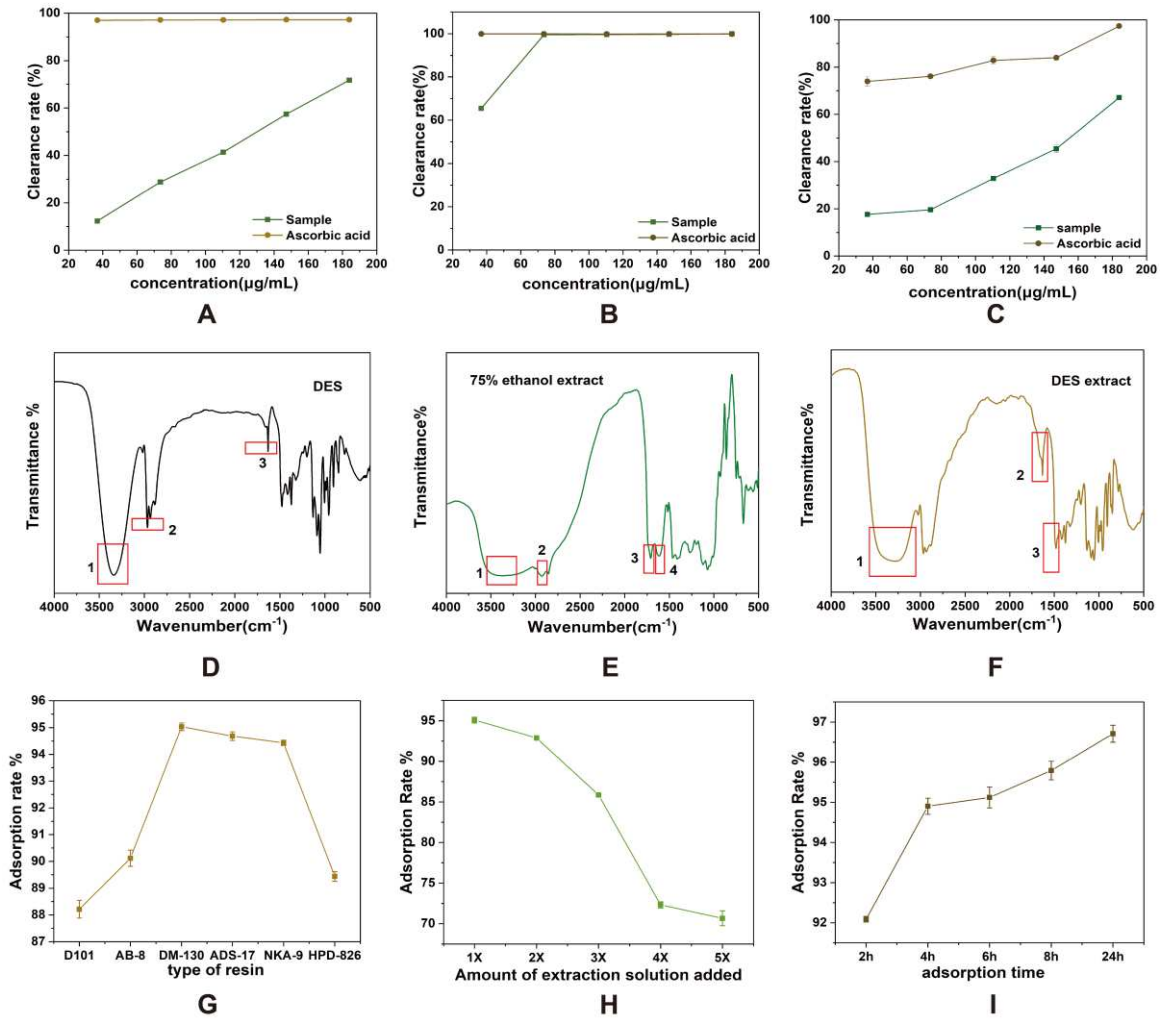


Fig.3 Evaluation of the DES Extraction Process (n=3)

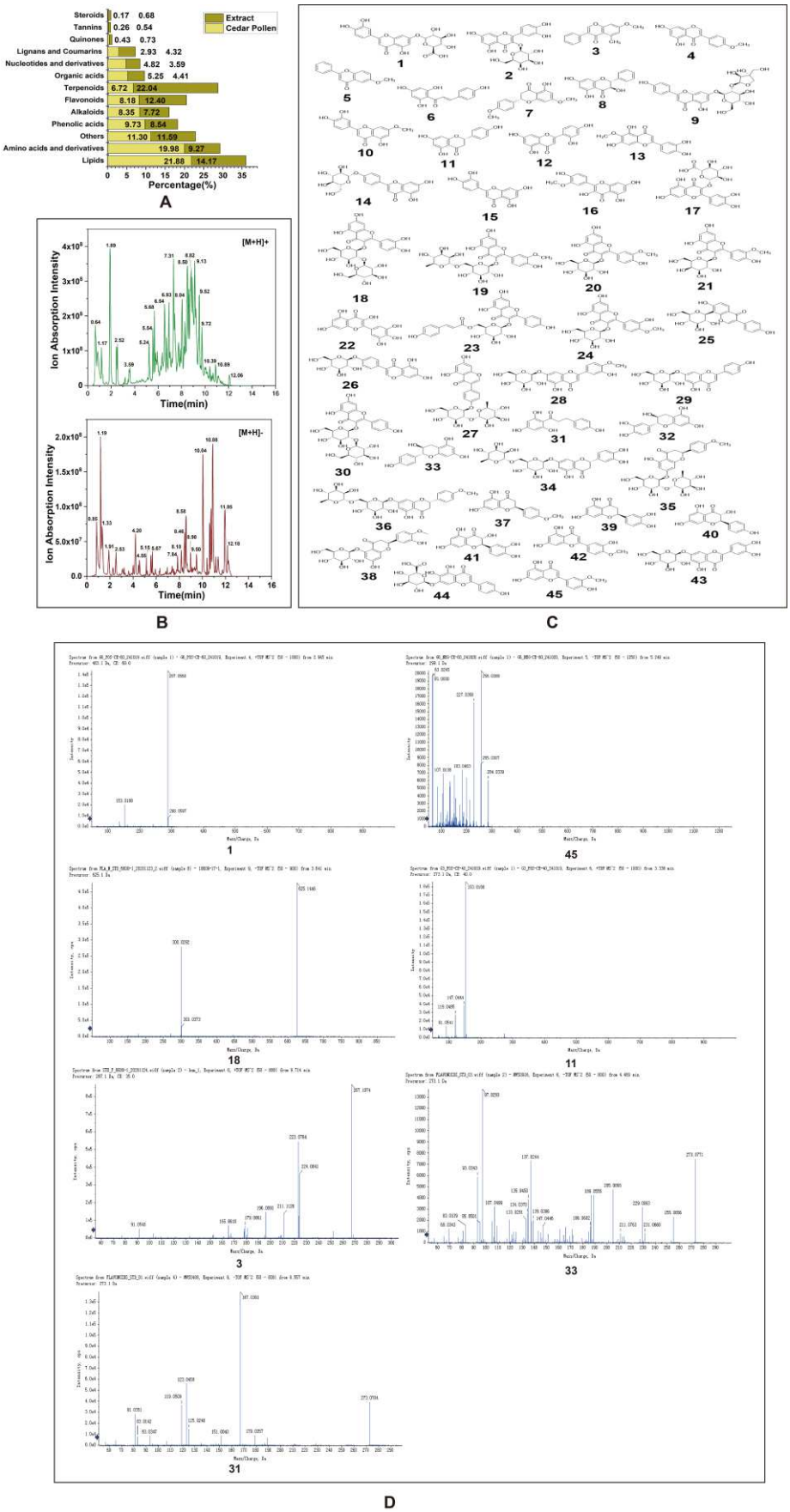


Fig.4 Diagram of off-target metabolomics and quantitative analysis of flavonoids

(A) Classification of compounds; (B) Positive and negative ion chromatograms of extracts;

(C) Compound structures; (D)Secondary mass spectra of representative components

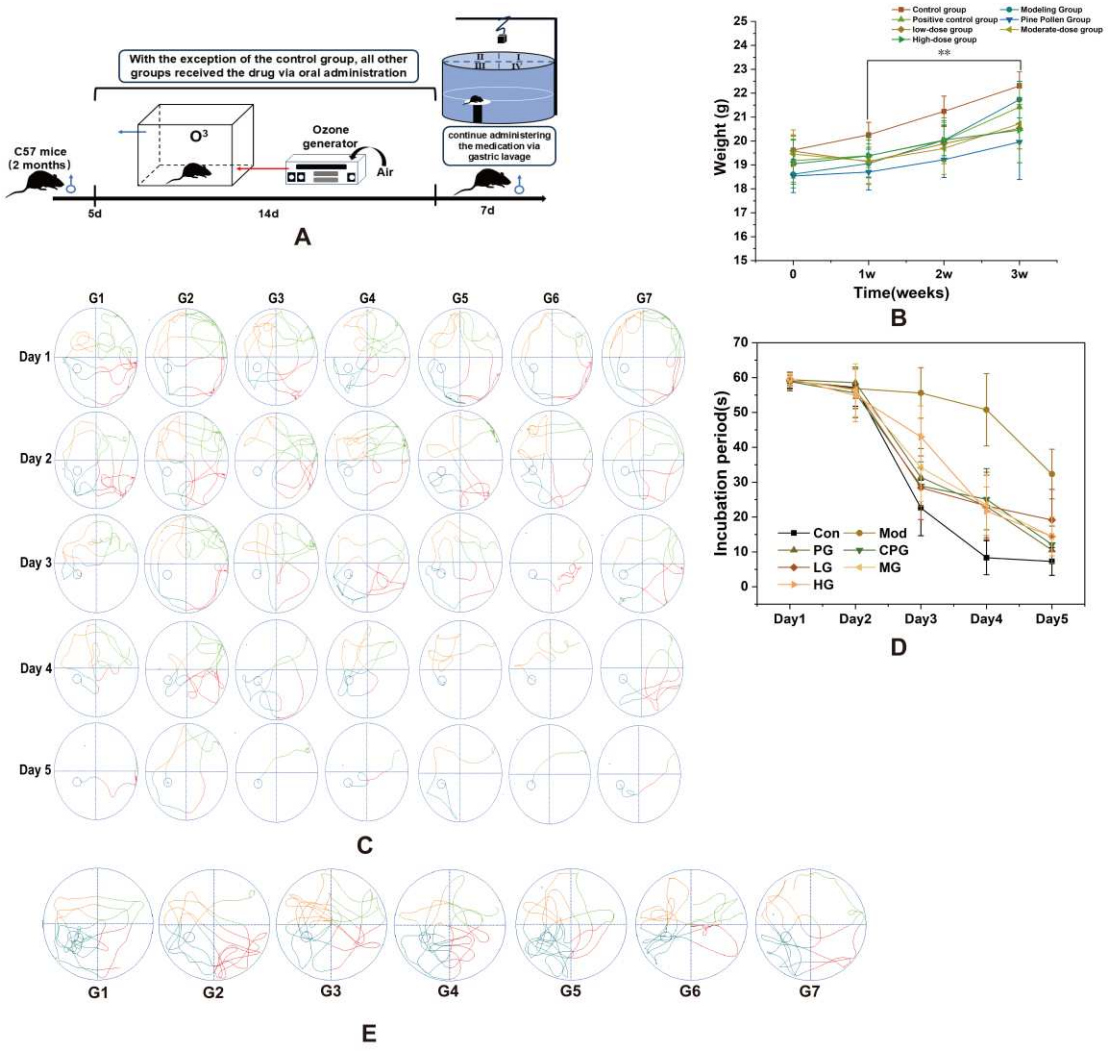


Fig.5 Diagram of the Morris Water Maze Experiment (n=10)

G1-Con；G2-Mod；G3-PG；G4-CPG；G5-LG；G6-MG；G7-HG

Control group (Con); Model group (Mod); Positive drug control group (PG); Cedar pollen group (CPG); Low-dose total flavonoids group (LG); Medium-dose total flavonoids group (MG); High-dose total flavonoids group (HG); same applies below

$^{*}p < 0.05$, $^{**}p < 0.01$ compared with the control group; $^{\#}p < 0.05$, $^{\#\#}p < 0.01$ compared with the model group

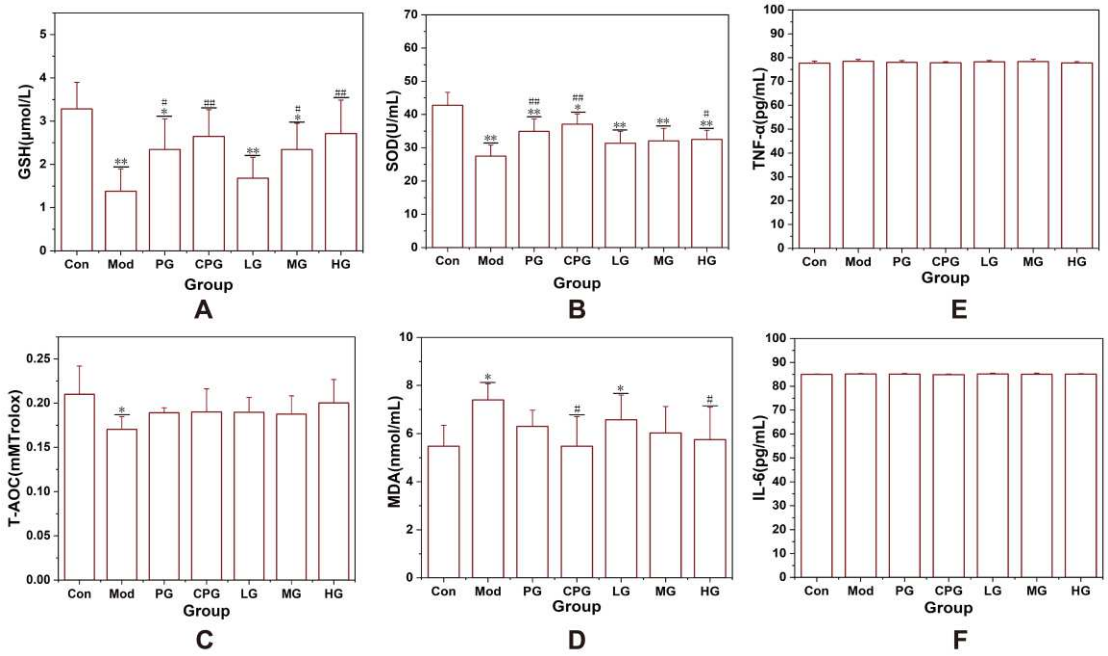
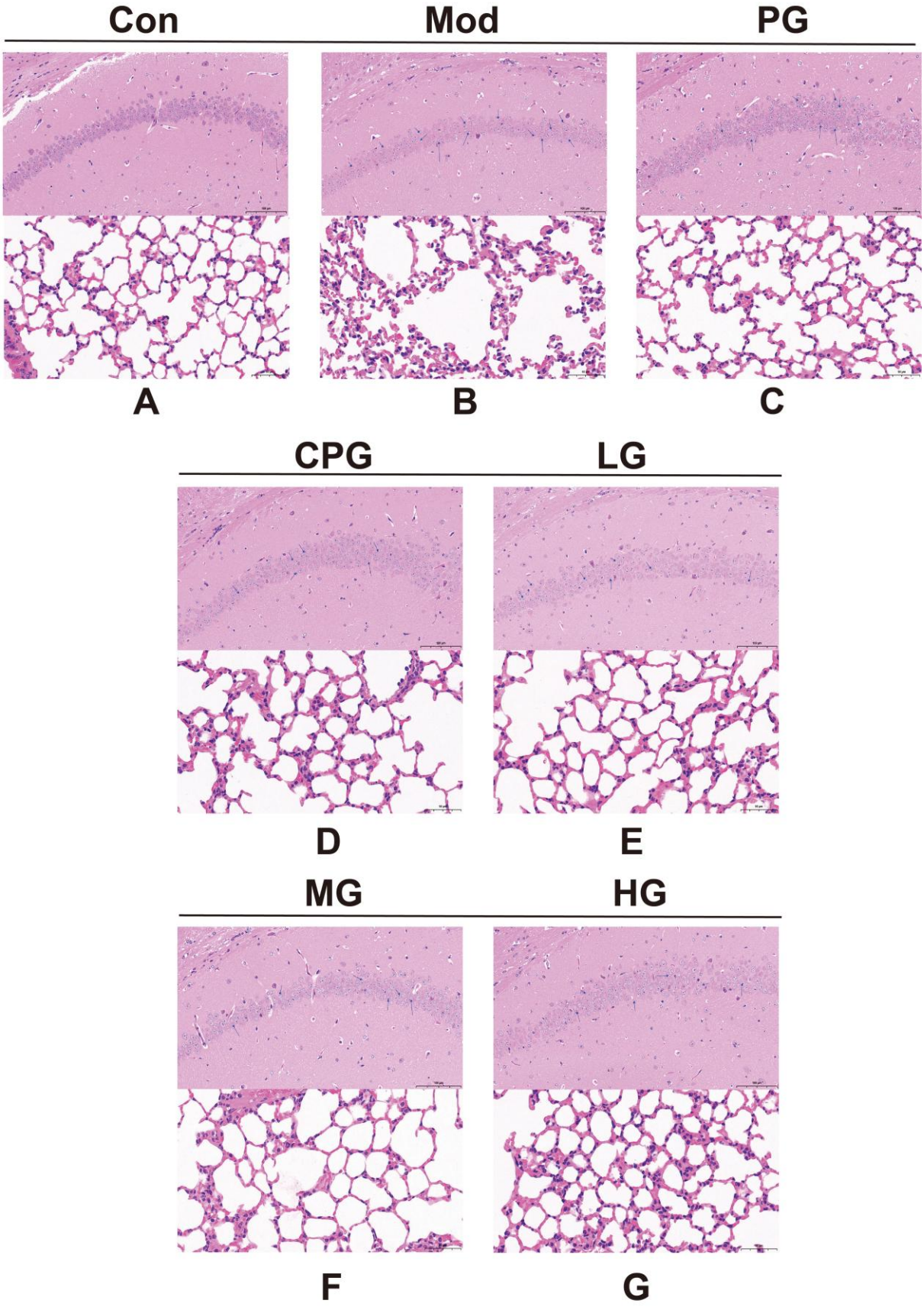


Fig.6 The Effects of Oxidative Stress and Inflammation-Related Markers (n=10)

$^{*}p < 0.05$, $^{**}p < 0.01$ compared with the control group; $^{\#}p < 0.05$, $^{\#\#}p < 0.01$ compared with the model group



1352 Fig.7 HE staining results of mouse brain and lung tissues (n=3)

brain tissue（100μm）；lung tissue（50μm）

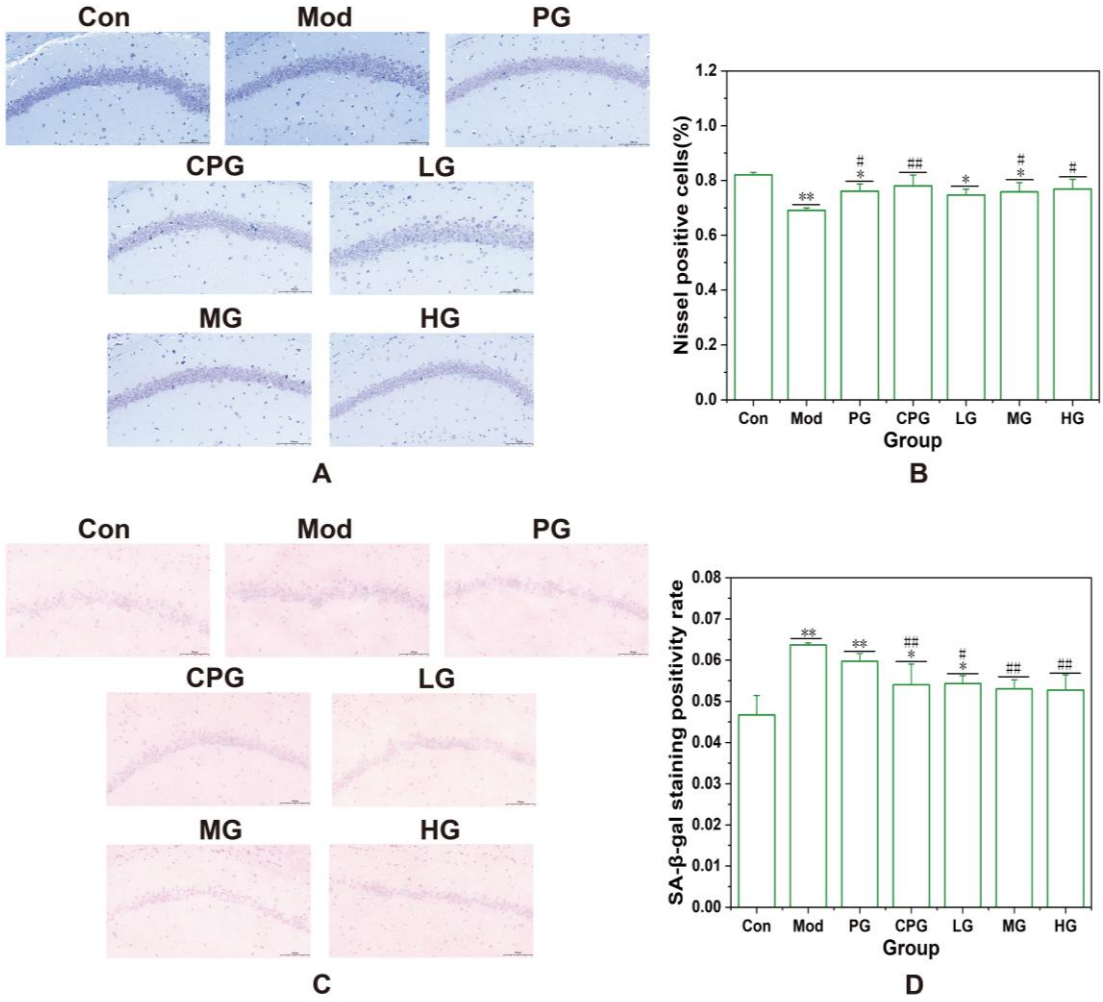
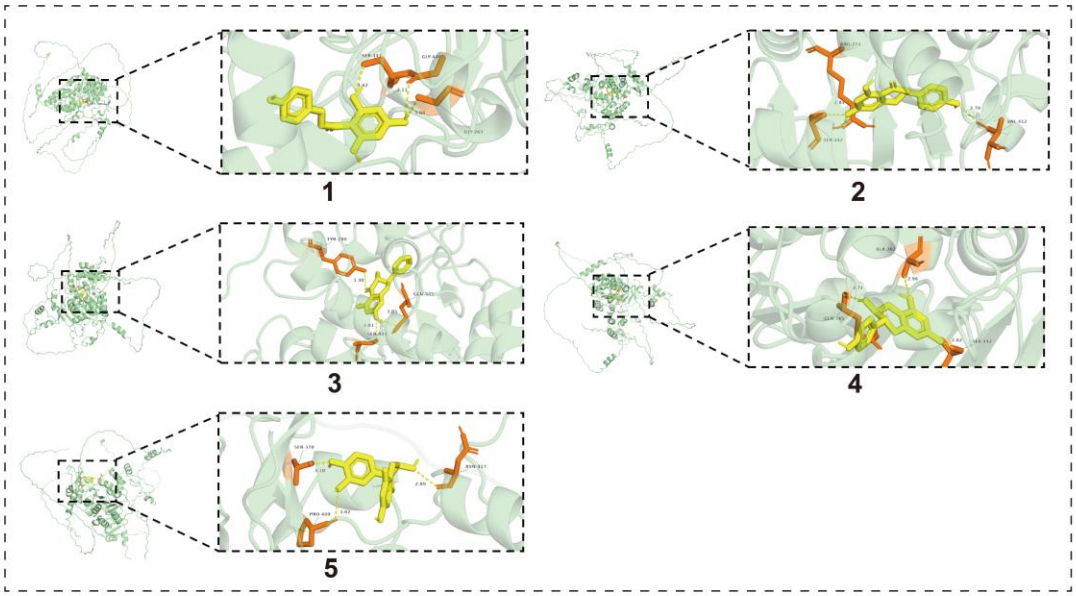
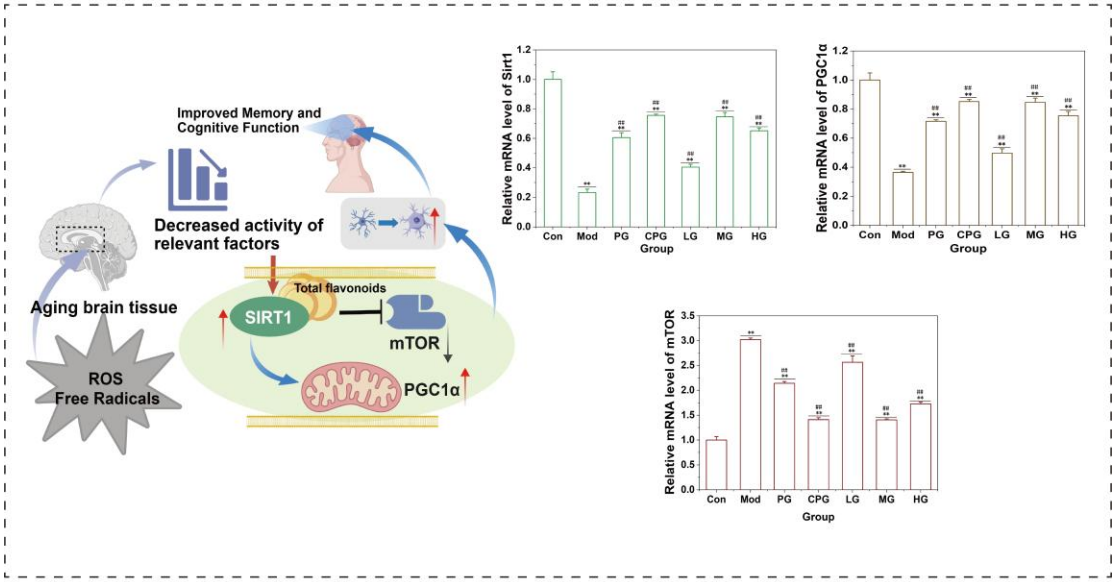


Fig.8 Results of Nissl and SA-β-gal staining of mouse brain tissue (n=3)

$^{*}p < 0.05$, $^{**}p < 0.01$ compared with the control group; $^{\#}p < 0.05$, $^{\#\#}p < 0.01$ compared with the model group



A



B

Fig.9 Molecular Docking and Detection of Related Molecular Expression

(A) Results of molecular docking between the representative compound and SIRT1;

(B) Relationship between aging and the expression of SIRT1, mTOR, and PGC-1α, and their key RNA expression in brain tissue

Supplementary Files

This is a list of supplementary files associated with this preprint. Click to download.

- GraphicalSummary.pdf
- Highlights1.docx
- CoverLetter.docx